UNIVERSITY OF CALIFORNIA, SAN DIEGO

Modeling, characterization and computational image processing for fiber-coupled imaging

A dissertation submitted in partial satisfaction of the
requirements for the degree
Doctor of Philosophy

in

Electrical Engineering (Photonics)

By

Nojan Motamedi

Committee in charge:

Professor Vitaliy Lomakin, Chair
Professor Joseph E. Ford, Co-Chair
Professor Prabhakar Rao Bandaru
Professor Yeshaiahu Fainman
Professor Donald James Sirbuly

2016

The Dissertation of Nojan Motamedi is approved, and it is acceptable in quality and form for publication on microfilm and electronically:

Co-Chair

Chair

University of California, San Diego

2016

DEDICATION

This dissertation is dedicated to my family for all their love and support.

TABLE OF CONTENTS

LIST OF FIGURES

LIST OF TABLES

ACKNOWLEDGEMENTS

I would like to thank my advisor, Professor Vitaliy Lomakin for his invaluable knowledge and support of my PhD study. I would also like to express my gratitude to my co-advisor Prof. Joseph E. Ford for his support of my graduate studies. Besides, I would like to thank the rest of my thesis committee: Prof. Yeshaiahu Fainman, Prof. Prabhakar Rao Bandaru, and Prof. Donald James Sirbuly for their helpful comments and encouragement. My sincere thanks goes to Dr. Mark A. Neifeld from University of Arizona for his invaluable discussions and suggestions.

I thank my colleagues at Photonic Systems Integration laboratory for their helpful discussions and all the fun we have had in the last four years.

Finally I would like to thank my wife, my parents, my sister and brothers for their constant support throughout my entire education.

Chapter 2, in full, is a reprint of the material as it appears in "Efficient analysis of deep high-index-contrast gratings under arbitrary illumination", Motamedi, Nojan; Shlivinski, Amir; Ford , Joseph E.; Lomakin, Vitaliy, *Optics express* 23, no. 26 (2015): 33472-33483. The dissertation author was the primary investigator and author of this paper.

Chapter 3, in full, is a reprint of the material as it appears in "Analysis and characterization of high-resolution and high-aspect-ratio imaging fiber bundles", Motamedi, Nojan; Karbasi, Salman; Ford , Joseph E.; Lomakin, Vitaliy, *Applied optics* 54, no. 32 (2015): 9422-9431. The dissertation author was the primary investigator and author of this paper.

Chapter 4, in part, has been submitted for publication of the material as it may appear in "Image restoration in fiber-coupled imagers using space-variant impulse response characterization", Motamedi, Nojan; Lomakin, Vitaliy; Ford , Joseph E. The dissertation author was the primary investigator and author of this paper.

Research documented in Chapters 2, 3 and 4 of this dissertation was supported by the DARPA SCENICC program under contract W911NF-11-C-0210.

VITA

2006 Bachelor of Science, University of Mazandaran

2009 Master of Science, Sharif University of Technology

2012 Master of Science, University of Central Florida, Orlando

2016 Doctor of Philosophy, University of California, San Diego

PUBLICATIONS

Nojan Motamedi, Vitaliy Lomakin, and Joseph E. Ford, “Image restoration in fiber-coupled imagers using space-variant impulse response characterization”, (under review).

Nojan Motamedi, Amir Shlivinski, Joseph E. Ford, and Vitaliy Lomakin. "Efficient analysis of deep high-index-contrast gratings under arbitrary illumination." *Optics express* 23, no. 26 (2015): 33472-33483.

Nojan Motamedi, Salman Karbasi, Joseph E. Ford, and Vitaliy Lomakin. "Analysis and characterization of high-resolution and high-aspect-ratio imaging fiber bundles." *Applied optics* 54, no. 32 (2015): 9422-9431.

Salman Karbasi, Igor Stamenov, Nojan Motamedi, Ashkan Arianpour, Adam R. Johnson, Ron A. Stack, Chris LaReau et al. "Curved fiber bundles for monocentric lens imaging." In *SPIE Optical Engineering+ Applications*, pp. 95790G-95790G. International Society for Optics and Photonics, 2015.

Salman Karbasi, Nojan Motamedi, Ashkan Arianpour, William M. Mellette, and Joseph E. Ford. "Analysis and compensation of moiré effects in fiber-coupled image

sensors." In *SPIE Optical Engineering+ Applications*, pp. 957910-957910. International Society for Optics and Photonics, 2015.

Salman Karbasi, Ashkan Arianpour, Nojan Motamedi, William M. Mellette, and Joseph E. Ford. "Quantitative analysis and temperature-induced variations of moiré pattern in fiber-coupled imaging sensors." *Applied optics*54, no. 17 (2015): 5444-5452.

Joseph E. Ford, Igor Stamenov, Salman Karbasi, Ashkan Arianpour, Nojan Motamedi, Ilya Agurok, Ron Stack et al. "Panoramic imaging via curved fiber bundles." In *Imaging Systems and Applications*, pp. ITh1A-4. Optical Society of America, 2015.

Ashkan Arianpour, Nojan Motamedi, Ilya P. Agurok, and Joseph E. Ford. "Enhanced signal coupling in wide-field fiber-coupled imagers." *Optics express* 23, no. 4 (2015): 5285-5299.

Stephen J. Olivas, Michal Šorel, Ashkan Arianpour, Igor Stamenov, Nima Nikzad, Glenn M. Schuster, Nojan Motamedi et al. "Digital image processing for wide-angle highly spatially variant imagers." In *SPIE Optical Engineering+ Applications*, pp. 91930B-91930B. International Society for Optics and Photonics, 2014.

Stephen J. Olivas, Nima Nikzad, Igor Stamenov, Ashkan Arianpour, Glenn Schuster, Nojan Motamedi, William M. Mellette et al. "Fiber bundle image relay for monocentric lenses." In *Computational Optical Sensing and Imaging*, pp. CTh1C-5. Optical Society of America, 2014.

Ashkan Arianpour, Ilya Agurok, Nojan Motamedi, and Joseph E. Ford. "Enhanced Field of View Fiber Coupled Image Sensing." In *International Optical Design Conference*, pp. IM2A-4. Optical Society of America, 2014.

Joseph E. Ford, Igor Stamenov, Stephen J. Olivas, Glenn Schuster, Nojan Motamedi, Ilya P. Agurok, Ron Stack, Adam Johnson, and Rick Morrison. "Fiber-coupled

monocentric lens imaging." In *Computational Optical Sensing and Imaging*, pp. CW4C-2. Optical Society of America, 2013.

ABSTRACT OF THE DISSERTATION

Modeling, characterization and computational image processing for fiber-coupled imaging

by

Nojan Motamedi

Doctor of Philosophy in Electrical Engineering (Photonics)

University of California, San Diego, 2016

Professor Vitaliy Lomakin, Chair

Professor Joseph E. Ford, Co-Chair

High-contrast imaging Fiber Bundles (FB) have been used in recent years to integrate high resolution, compact and wide field-of-view imagers into small volumes. Imaging fiber bundles are composed of arrays of individual high-contrast optical fibers that are fused together to form a uniform and reliable image-transfer medium. Monocentric lenses have been designed to demonstrate superior diffraction-limited

performance in the visible spectrum with few optical elements which enables integration of robust imagers into a small volume. However the curved image plane formed by these lenses can not be detected with conventional flat image sensors. Additional optical elements can be introduced to flatten the image plane but it would lead to the complexity of the system design and loss of compactness. One can instead take advantage of imaging fiber bundles to overcome this limitation. FBs can be milled and polished to form a curved input facet and a flat output facet to map the spherical image plane onto the flat image sensor plane. Proper understanding of imaging fiber bundles performance is therefore crucial for designing a low cross-talk image-transfer medium.

In this dissertation the Rigorous Coupled Wave Analysis (RCWA) method is used for 2D (1D+propagation) modeling of deep periodic dielectric gratings (straight imaging fiber bundles) and a numerical method is presented to efficiently calculate the electromagnetic beam transmission through the arrays of fibers. The Scanning Electron Microscope (SEM) image of the straight FB cross-section is captured and processed to extract the actual core boundaries. The measured core boundaries are then used for 3D (2D+propagation) modal analysis of fiber bundles. The effect of irregularity is also investigated in both 2D and 3D models and it is shown to improve the light confinement and image transfer fidelity in optical fiber bundles. The straight fiber bundles with various pitches are then experimentally characterized to measure the performance under different illumination conditions. A performance metric is used to quantify cross-talk in fiber bundles and demonstrate the poor performance in the

fibers with core pitches of only a few wavelengths of the guided light. The experimental measurements are then compared to numerical modeling results and are shown to be in good agreement. The numerical and experimental modeling is followed by an experimental measurement of a fiber-coupled imager (FCI) in order to restore the lost resolution due to problems associated with fiber-sensor coupling. The Point Spread Function (PSF) of the strongly shift-variant FCI is first measured as a function of input location with sub pixel spatial resolution. Various computational image reconstruction methods are then used to recover the captured image resolution to that of the fiber bundle pitch.

Chapter 1 Introduction

The design of conventional imaging systems with wide field-of-view typically requires multiple number of optical elements to flatten the image plane and minimize aberrations in the detected image. Flat image sensors are available in these scenarios to capture the image, however this will lead to a bulky system that is not compact. To overcome the compactness problem, one can instead take advantage of monocentric lenses, in which fewer number of optical elements are required to form the high quality image. The image plane is not flat in these cases and a curved image sensor with proper radius of curvature is needed for capturing the image. The current semiconductor technology is mature for planar fabrication processes, yet little progress has been made for non-planar realization. The available curved image sensors either have large radius of curvature or more importantly have low resolution. One can use

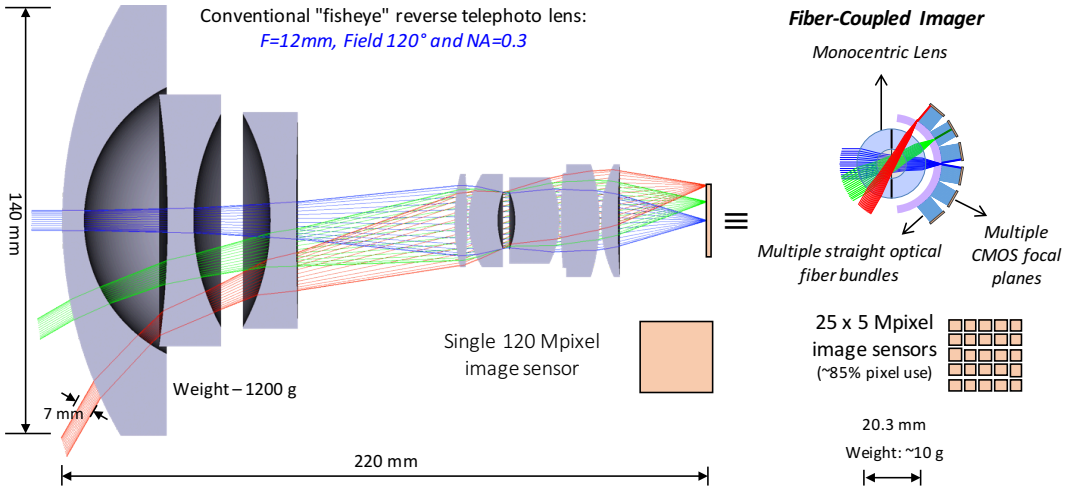

Figure 1-1 Comparison of the conventional wide-field-of-view fish eye lens and the monocentric fiber-coupled imager with comparable performance.

imaging fiber bundles, an array of high-index-contrast optical fibers, which are fused together to form an image transfer medium. Imaging Fiber bundles were initially used for image transfer and illumination applications. Nowadays they are used for various applications including endoscopy, optical coherence tomography, illumination, optical switching and optical inspection. Recently they have been used along with monocentric lenses to transfer the image formed on the curved image plane onto the flat image sensor plane. Straight and tapered (curved) fiber bundles can be milled and polished to form a high quality and optically flat surface that minimizes light scattering. This enables the realization of monocentric lens imaging using high resolution imaging fiber bundles.

The underlying assumption in utilizing imaging fiber bundles for fiber-coupled imaging applications is that the cross-talk between individual fibers is negligible otherwise a blurred image will be detected by the image sensor. Proper analysis and design of imaging fiber bundles is therefore crucial for these applications. In this

dissertation the numerical electromagnetic modeling of fiber bundles is investigated both in 2D and 3D. The effect of fiber's structural parameters including the size, shape and complex refractive index of core, cladding and absorbing material as well as the impact of irregularity between fibers is studied. The numerical modeling is followed by experimental characterization of imaging fiber bundles with various pitches. At the end a fiber-coupled image sensor is characterized to measure its Point Spread Function (PSF) as a function of input probe location. The PSF map is then used to restore the captured image in the region of interest.

Chapter 2 discusses the 2D (1D periodic + propagation) numerical analysis of imaging fiber bundles. Rigorous Coupled Wave Analysis (RCWA) is used to model the imaging fiber bundle as a 2D grating with 1D periodicity. An analytical method is presented for computing the problem of an electromagnetic beam transmission through deep periodic dielectric gratings. In this method the incident beam is decomposed into the plane waves spectrum, transmission coefficients corresponding to each such plane wave are found via RCWA, and the transmitted beam is calculated via inverse Fourier integral. To make the approach efficient for deep gratings the fast variations of the transmission coefficients versus spatial frequency are calculated analytically by casting the summations and integrals in a form that has explicit rapidly varying exponential terms. The presented formulation allows computing the transmitted beam with a smaller number of samples independent of the grating depth.

Chapter 3 discusses the electromagnetic modeling of imaging fiber bundles in 3D (2D + propagation) along with experimental characterizations to quantify the

cross-talk between fibers for various pitches. Scanning Electron Microscope (SEM) images of fiber bundles cross-section are taken to measure the physical parameters and verify the variations of irregular fibers due to the fabrication process. A modal analysis tool is developed to include irregularities in the fiber core shapes and provide results in agreement with experimental measurements. The modeling demonstrates that the irregular fibers significantly outperform a perfectly regular "ideal" array. Using this method, fiber bundles are designed that can provide high contrast with core pitches of only a few wavelengths of the guided light. It is shown that structural modifications of the commercially available fiber bundle can reduce the core pitch by 60% for higher resolution image relay.

Chapter 4 is dedicated to the characterization of a fiber-coupled image (FCI) sensor in a limited region of interest followed by image restoration of the blurred captured image. These type of imagers suffer from defects and fiber-sensor misalignment which would introduce defects and moiré pattern as well as image blur and loss of resolution due to the unwanted gap between fiber bundle and the image sensor. The PSF map of the strongly shift-variant FCI is measured as a function of input location in order to recover the lost resolution up to the fiber pitch with computational image processing techniques.

Chapter 2 Rigorous Coupled Wave Analysis of Deep 2D Fiber Bundles

2-1 Introduction

An efficient method for computing the problem of an electromagnetic beam transmission through deep periodic dielectric gratings is presented in this chapter. In this method the beam is decomposed into a spectrum of plane waves, transmission coefficients corresponding to each such plane wave are found via Rigorous Coupled Wave Analysis, and the transmitted beam is calculated via inverse Fourier integral. To make the approach efficient for deep gratings the fast variations of the transmission coefficients versus spatial frequency are accounted for analytically by casting the summations and integrals in a form that has explicit rapidly varying exponential terms.

The resulting formulation allows computing the transmitted beam with a small number of samples independent of the grating depth.

Dielectric gratings are used in numerous applications. One example is "imaging fiber bundle", an array of parallel dielectric fibers, where each fiber is a high index multimode waveguide surrounded by a lower index cladding (Figure 2-1). Such fiber bundles (FB) provide a non-imaging transfer of the spatial distribution of light between two surfaces, with applications such as endoscopic imaging [1,2] and image sensing of a curved input surface [3] to name but a few. The ability to efficiently and accurately model such structures is becoming increasingly important. This is especially true as applications emerge with the spatial period of the fiber structure and the image sensor being on the order of a few microns [4-6]. Accurate and efficient modeling of the spatial resolution of the FB is complicated due to the energy transfer between its modes [7-9] as the extended guided modes interfere strongly as the depth of grating increases.

Often, the fibers in the bundle can be considered periodic or periodic with multiple fibers per period. The excitation may be a plane wave, but more often the excitation is a beam or a spatially modulated image. When the bundle is considered to be periodic, the computational problem is one having a periodic geometry with an aperiodic excitation. Several methods can be adapted to numerically model such deep gratings [9-13]. One possible approach is to use coupled mode analysis [14,15] but it makes approximations in terms of neglecting the propagating spectrum. Another approach is the Fourier decomposition of the incident field [16], in which the incident

field is decomposed into a spectrum of plane waves. For each such plane wave the problem becomes completely periodic. The transmitted diffraction orders can be calculated for each wavenumber using a periodic solver, e.g. Rigorous Coupled Wave Analysis (RCWA) [17,18]. Transmitted output field is then calculated by taking the inverse Fourier transform of the transmitted field for each diffraction order. However, using this approach becomes complicated for very deep gratings. The difficulties arise from the fact that the transmitted diffraction orders have fast phase variations in their wavenumber dependence, which are associated with the large propagation range.

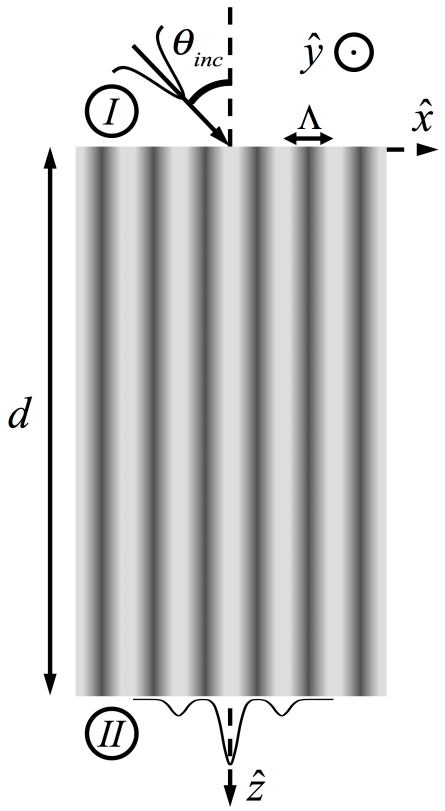

Figure 2-1 Schematic of the problem: deep periodic structure illuminated with arbitrary incident beam.

Fourier decomposition of the incident field has been used along with Rigorous Coupled Wave Analysis [16] to analyze the scattering of a confined beam off a periodic structure. In this method, the incident beam is decomposed into a spectrum of plane waves, the transmission coefficients corresponding to these plane waves are calculated using the Floquet theorem via RCWA, and the final transmitted beam is computed from the inverse Fourier integral. However, such an approach results in a large computational cost for very deep gratings. In this paper we propose an alternative method, using the analytic property of Bloch waves propagation in the grating region to compute the transmitted field with a much smaller number of samples in deep gratings. This computationally efficient method requires keeping track of individual Bloch waves created at the input facet of the grating. The method neglects the insignificant multiple internal scattering of Bloch waves in the grating region. The resulting Bloch wave excitation coefficients and the corresponding components in the transmitted field vary slowly as a function of the angle (or wavenumber). Using the slow variation property, we developed a semi-analytical method that computes the transmitted field using FFTs with a much smaller number of samples. This number of samples is nearly independent of the grating depth. The result is a major computational speed up, which enables fast computations of the transmitted fields in very deep gratings. The paper is organized as follows. Section 2 provides problem statement. Section 3 presents the numerical formulation describing all the steps for efficiently computing the transmitted beam. Section 4 presents numerical

results supporting the numerical formulation. Section 5 summarizes and discusses the findings.

2-2 Problem Statement

Consider a grating composed of a dielectric material with a complex permittivity that is periodic in the x direction with period (Figure 2-1). Each period can comprise only a single fiber or multiple fibers, typically with a random position. The grating depth (d) is much greater than the period or the wavelength with typical values of tens of thousand of wavelength. A TE-polarized optical beam with the electric field in the y-direction is incident on the grating from the top. The incident beam is coupled into a set of guided modes of the grating. The set of guided modes propagate through the structure and are coupled into the transmitted beam propagating downwards.

The considered structure is periodic but the exciting beam is aperiodic. The beam, however, can be decomposed into a continuum of plane waves via Fourier transform. For each such plane wave both the excitation and the structure are periodic. For such a periodic problems the Floquet theorem can be used to represent the solution in terms of a discrete set of plane waves. Furthermore, the rigorous coupled wave analysis (RCWA) can be used to find the coefficients of the scattered plane waves, excited (Bloch) waves in the grating, and the transmitted field. This RCWA solution can be further simplified by utilizing the fact the grating is very deep and neglecting the multiple bounces of the grating Bloch waves between the entrance and exit

interfaces. As a result, the problem is reduced into three parts: coupling into the grating at the entrance interface, propagating from the entrance to the exit interface, and coupling out of the grating at the exit interface. Once the coefficients of each plane wave corresponding to the incident beam decomposition are found the resulting transmitted beam is calculated via Fourier transform. The following important components need to be addressed to allow efficiently solving this numerical problem: (i) computing the coupling (scattering, reflection, transmission) coefficients, (ii) calculating the Bloch waves, and (iii) computing the Fourier decomposition integral for the transmitted beam with a small number of samples even at very large propagating distances. These aspects are addressed in the next section.

2-3 Formulation

2-3-1 Global RCWA Formulation

The electric field of the incident beam at the entrance interface can be represented via a continuous Fourier decomposition

$$E^{in}(x) = \frac{1}{2\pi}\int \hat{E}^{in}(k_x)e^{-jk_x x}\,dk_x\,, \tag{1}$$

where

$$\hat{E}^{in}(k_x) = \int E^{in}(x)e^{jk_x x}\,dk_x\,, \tag{2}$$

represents coefficients of the incident beam's plane wave spectrum. Once the plane wave spectrum of the incident wave is known the Floquet theorem can be applied to calculate the scattered fields (reflected and transmitted) via diffraction coefficients for the periodic structure. The diffraction coefficients are found by matching the electric and magnetic fields at input and output interfaces using a set of forward and backward Bloch waves for the grating region. We start with a summary of the general RCWA procedure [17],[18] and simplify it to account for the decoupling between the entrance and exit interfaces due to the large depth of the structure. The periodic permittivity is first expanded via the Fourier series

$$\varepsilon(x) = \sum_m \varepsilon_m \exp\left(j \frac{2\pi m}{\Lambda} \right), \tag{3}$$

where $\varepsilon_m = \Lambda^{-1} \int^{\Lambda} \varepsilon(x) \exp\left(-jx 2\pi m/\Lambda\right) dx$ is the Fourier series coefficient of the complex permittivity and Λ is the period of the grating. Using the Floquet theorem the fields in regions I and II are written as

$$\begin{aligned} E^{I,y}(x,z) &= E^{in,y}(x,z) + \sum_i R_i \exp\left[-j\left(k_{xi} x - k_{I,zi} z \right) \right] \\ E^{II,y}(x,z) &= \sum_i T_i \exp\left\{ -j\left[k_{xi} x - k_{II,zi} \left(z - d \right) \right] \right\}, \end{aligned} \tag{4}$$

where R_i is the reflection coefficient in region I and T_i is the transmission coefficients in region II, $k_{x,i} = k_x - iK$, $K = \frac{2\pi}{\Lambda}$. The wavenumbers $k_{I,zi}$ and $k_{II,zi}$ are given by

$$k_{l,zi} = \begin{cases} +k_0\left[n_l^2 - (k_{xi}/k_0)^2\right]^{1/2} & k_0 n_l > k_{xi} \\ -jk_0\left[(k_{xi}/k_0)^2 - n_l^2\right]^{1/2} & k_0 n_l < k_{xi} \end{cases}, \quad l = I, II. \tag{5}$$

The electric and magnetic fields inside the grating region can be written using a set of forward and backward Bloch waves

$$\begin{aligned} E^{gy} &= \sum_i \sum_m w_{i,m} \left\{ c_m^+ \exp\left(-k_0 q_m z\right) + c_m^- \exp\left[k_0 q_m \left(z-d\right)\right] \right\} \exp\left(-jk_{xi} x\right) \\ H^{gy} &= -j\left(\varepsilon_0/\mu_0\right) \sum_i \sum_m v_{i,m} \left\{ -c_m^+ \exp\left(-k_0 q_m z\right) + c_m^- \exp\left[k_0 q_m \left(z-d\right)\right] \right\} \exp\left(-jk_{xi} x\right), \end{aligned} \tag{6}$$

where q_m and $w_{i,m}$ are the square root of the eigenvalues with a positive real part and the (i,m) element of the eigenvector matrix W of matrix $\mathbf{A} = (k_{xi}/k_0)^2 - E$ for the TE polarization. $\boldsymbol{E}$ is the Toeplitz permittivity matrix with its (i,m) element being ε_{i-m}. The quantity $v_{i,m} = q_m w_{i,m}$ is the (i,m) element of the matrix product $V = WQ$, where Q is a diagonal matrix with elements q_m. The coefficients c_m^+ and c_m^- are the amplitudes of the forward and backward Bloch waves yet to be determined within the grating region. The summations over the diffraction order index i is over an infinite set of positive and negative integers and the summation over Bloch wave index m is over an infinite set of positive integers. These infinite summations are truncated to finite numbers for a numerical implementation. Using equation sets (4) and (6) one can match the electric and magnetic fields at input and output interfaces to obtain the following system of equations

$$\begin{aligned}
&\delta_{i0} + R_i = \sum_m w_{i,m} \left\{ c_m^+ + c_m^- \exp\left(-k_0 q_m d\right) \right\} \\
&j\left[\delta_{i0} \cos(\theta) n_I - \left(k_{I,zi} / k_0 \right) R_i \right] = \sum_m v_{i,m} \left\{ c_m^+ - c_m^- \exp\left(-k_0 q_m d\right) \right\},
\end{aligned} \tag{7}$$

$$\begin{aligned}
&\sum_m w_{i,m} \left\{ c_m^+ \exp\left(-k_0 q_m d\right) + c_m^- \right\} = T_i \\
&\sum_m v_{i,m} \left\{ c_m^+ \exp\left(-k_0 q_m d\right) - c_m^- \right\} = j\left(k_{II,zi} / k_0 \right) T_i ,
\end{aligned} \tag{8}$$

where δ_{i0} is the Kronecker delta function. Equations (7) and (8) can be solved simultaneously to calculate the scattered diffraction orders, which is the complete rigorous solution of the plane wave scattering from the periodic structure known as RCWA. We refer to this complete solution as Global RCWA (G-RCWA) in the rest of the paper.

2-3-2 Forward RCWA Formulation

The coupling between the forward and backward waves can be weak, e.g. due to losses, scattering, or weak reflections at the interfaces, as in the case of deep transmissive gratings or imaging fiber bundles [[4]-[6]]. In this case, the equation sets (7) and (8) are decoupled and may be solved separately, which is equivalent to neglecting the coupling between the forward and backward Bloch waves with coefficients c_m^+ and c_m^-. The result is a two-step solution procedure for calculating the diffraction coefficients, which we refer to as Forward RCWA (F-RCWA). In the first

step of F-RCWA, the input single-interface scattering coefficients c_m^+, are found via the following equation set [Eq. (7) by neglecting c_m^-]

$$\begin{aligned} &\delta_{i0} + R_i = \sum_{m=1} w_{i,m} c_m^+ \\ &j\left[\delta_{i0}\cos(\theta) n_I - \left(k_{II,zi}/k_0\right) R_i\right] = \sum_m v_{i,m} c_m^+ . \end{aligned} \tag{9}$$

In the second step, the first interface's transmission coefficients c_m^+ are already known and give the amplitudes of the forward Bloch waves, which serve as an excitation for the second interface after propagating through the depth of grating. The scattering problem at the second interface is described by Eq. (8) with the known value of c_m^+, from which the amplitudes of the transmitted diffraction orders T_i are found for a given k_x. Once the transmission diffraction coefficients are found the output field may be written as

$$E^T(x) = \sum_i \int \hat{E}^{in}(k_x) T_i(k_x) e^{-jk_{x,i}x}\, dk_x , \tag{10}$$

where $T_i(k_x)$ is the transmitted diffraction order versus the wavenumber calculated in Eq. (8). The inverse Fourier integral may be evaluated directly via Discrete Fourier Transform (DFT). Fast Fourier Transform (FFT) can be used if the number of samples is chosen as a product of prime numbers. Therefore, one can rewrite Eq. (10) as

$$E^T(x) = \sum_i \sum_n \hat{E}^{in}(k_x) T_i(k_x) e^{-jk_{x,i}x} , \tag{11}$$

where $k_{x,i} = k_x - iK$ is the same as before with $k_x = n2\pi/L_x$ and L_x is the extent of calculations in x direction. If approached based on the Nyquist sampling criteria directly, the solution of Eq. (11) requires a very large number of samples for a very deep grating due to the fast phase variations of T_i as a function of k_x. These fast variations are due to the propagation factor $\exp(-k_0 q_m d)$ in Eq. (8) associated with the imaginary part of q_m and the long-range propagation of the Bloch waves. The transmission coefficient T_i is determined by the contribution of all Bloch waves and therefore, it is impossible to smooth its wavenumber dependence, due to its rapid variations and the large number of samples requirement.

2-3-3 Semi-analytical Approach

The effect of the rapid variations associated with the factor $\exp(-k_0 q_m d)$ can be accounted for analytically if $T_i(k_x)$ is written as a sum of partial transmission coefficient contributions corresponding to individual Bloch waves

$$T_i(k_x) = \sum_m \tilde{T}_{i,m}(k_x) e^{-k_0 q_m(k_x) d}. \tag{12}$$

Here, $\tilde{T}_{i,m}$ are the partial transmission coefficients determined by modifying Eq. (8)

$$\begin{aligned} w_{i,m} c_m^+ + \sum_{m'} w_{i,m'} \tilde{c}_{m,m'}^- &= \tilde{T}_{i,m}(k_x) \\ v_{i,m} c_m^+ - \sum_{m'} v_{i,m'} \tilde{c}_{m,m'}^- &= j(k_{II,zi}/k_0)\tilde{T}_{i,m}(k_x), \end{aligned} \tag{13}$$

where $\tilde{c}^{-}_{m,m'}$ are the modified Bloch wave reflection coefficients of the second interface as a response to the c^{+}_{m} Bloch wave excitation. An important feature of Eq. (13) as compared to Eq. (8) is that the set of Eq. (13) does not have the factor $\exp(-k_0 q_m d)$, i.e. $\tilde{T}_{i,m}$ and q_m are independent of the grating depth. As a result, the variations of $\tilde{T}_{i,m}$ and q_m with respect to the wavenumber k_x (angle) only depend on the wavelength and the permittivities, and therefore, are on a much slower scale than the variations of $T_i(k_x)$. However propagation of the Bloch waves form the input to the output interface in a deep grating still introduces fast phase variations in the summation terms of Eq. (12) explicitly via the factor $\exp(-k_0 q_m d)$. For this reason the accurate calculation of Eq. (11) would still require dense sampling if evaluated directly and purely numerically. However, one can use the fact that the factor $\exp(-k_0 q_m d)$ is known analytically to reduce the integral sampling rate and make it independent of the grating depth. To this end, one can substitute Eq. (12) into Eq. (10) to rewrite the transmitted field as

$$E^T(x) = \sum_i \sum_m \int \hat{E}^{in}(k_x)\tilde{T}_{i,m}(k_x) e^{-k_0 q_m(k_x)d} e^{-jk_{x,i}x}\, dk_x. \qquad (14)$$

The summation in Eq. (14) can be taken only over the propagating Bloch waves while the integrand is negligible for cutoff (decaying) Bloch waves. For propagating modes the integrand has two components, including the amplitude $\hat{E}^{in}(k_x)\tilde{T}_{i,m}(k_x)$ that is slowly varying function of k_x and the exponential

$\exp(-k_0 q_m d)$ that is rapidly varying for large propagation distances. However, in comparison to $\exp(-jk_{x,i}x)$, the exponential power related to q_m is a much slowly varying function of k_x. Therefore, one can tabulate the amplitude $\hat{E}^{in}(k_x)\tilde{T}_{i,m}(k_x)$ and the eigenvalues q_m at a coarse set of k_x samples, sufficient to resolve their behavior, e.g. by local interpolation. The tabulated values can further be used to calculate the Fourier integral in Eq. (14). To this end, the Fourier integral in Eq. (14) can be represented via a discrete sum of integrals

$$E^T(x) = \frac{1}{\Delta k_x} \sum_i \sum_m \sum_n \int_{k_{x_n}}^{k_{x_{n+1}}} \hat{E}^{in}(k_x)\tilde{T}_{i,m}(k_x) e^{\phi_{i,m,n}(k_x)} e^{-jk_{x,i}x}\, dk_{x_n}\,, \tag{15}$$

with $\phi_{i,m,n}(k_x) = -k_0 q_m(k_x) d$. First order Taylor expansion of the phase term can be used to evaluate the fast integrand $e^{\phi_{i,m,n}(k_x)}$ in Eq. (15) analytically.

$$I_{i,m,n} = \frac{1}{\Delta k_x} \int_{k_{xn}}^{k_{x_{n+1}}} e^{\phi_{i,m,n}(k_x)}\, dk_x = \frac{1}{\Delta k_x} \int_{k_{x_n}}^{k_{x_{n+1}}} e^{\left[\phi_{i,m,n}(k_{xn}) + \phi'_{i,m,n}(k_{xn}).(k_x - k_{xn})\right]}\, dk_x = e^{\phi_{i,m,n}(k_{xn})} \frac{e^{\phi'_{i,m,n}(k_{xn})\Delta k_x} - 1}{\Delta k_x \phi'_{i,m,n}(k_{xn})}\,. \tag{16}$$

Here $I_{i,m,n}$ is the result of piecewise analytical inverse Fourier integral. This way the fast integrand is computed accurately to the first order between the sampling points of the coarse table. The analytical evaluation of the fast integral also makes the calculations independent of the grating depth or propagation distance *d*, such that there

is no need for taking larger number of samples for deeper gratings. Substituting Eq. (16) into Eq. (15) yields

$$E^T(x) = \sum_i \sum_n \hat{E}^{in}(k_x) e^{-jk_{x,i}x} \sum_m \tilde{T}_{i,m,n} I_{i,m,n} \ . \tag{17}$$

The DFT summation over n in Eq. (17) is the most time consuming part of the calculations. Comparing Eq. (17) with Eq. (11) one should note that the summation over the Bloch waves (m) in Eq. (17) is already taken in Eq. (11). However, the inverse DFT summation in Eq. (11) is taken over a much larger number of samples compared to the same calculation in Eq. (17). The novelty in using Eq. (17) relies in taking the piecewise inverse Fourier transform analytically before summing up the contribution of the Bloch waves as opposed to Eq. (11). In other words, the scattering coefficients $\tilde{T}_{i,m}$ are weighted by $I_{i,m,n}$ before calculating the inverse DFT, which was performed by using the FFT algorithm. Since $I_{i,m,n}$ coefficients are calculated analytically from a simple function, the summation (m) is computed rapidly as compared to overall computation time.

2-4 Numerical Analysis and Results

We start with verifying that the F-RCWA approach compares well to the G-RCWA one. To that end, a straight grating (waveguide array) of 1.5 μm period and 1 *cm* depth was analyzed at a wavelength of 550 *nm* with the F-RCWA and G-RCWA solutions. The grating depth corresponded to 18,200 wavelengths and depth-period

ratio was 12,133. Schott's imaging fiber bundle's (FB) material [[19],[20]] was used to make the comparisons more realistic. The FB consisted of 30% cladding with refractive index of 1.48 and 70% core with refractive index of 1.81.

Figure 2-2(a) shows the total transmitted power calculated by G-RCWA and F-RCWA versus incident angle when the medium in region *II* is vacuum. Total transmitted power was calculated by summing up the transmitted diffraction orders.

The rapid fluctuations of the transmitted power can be observed in both calculated methods due to the fast variations of the exponential terms describing the

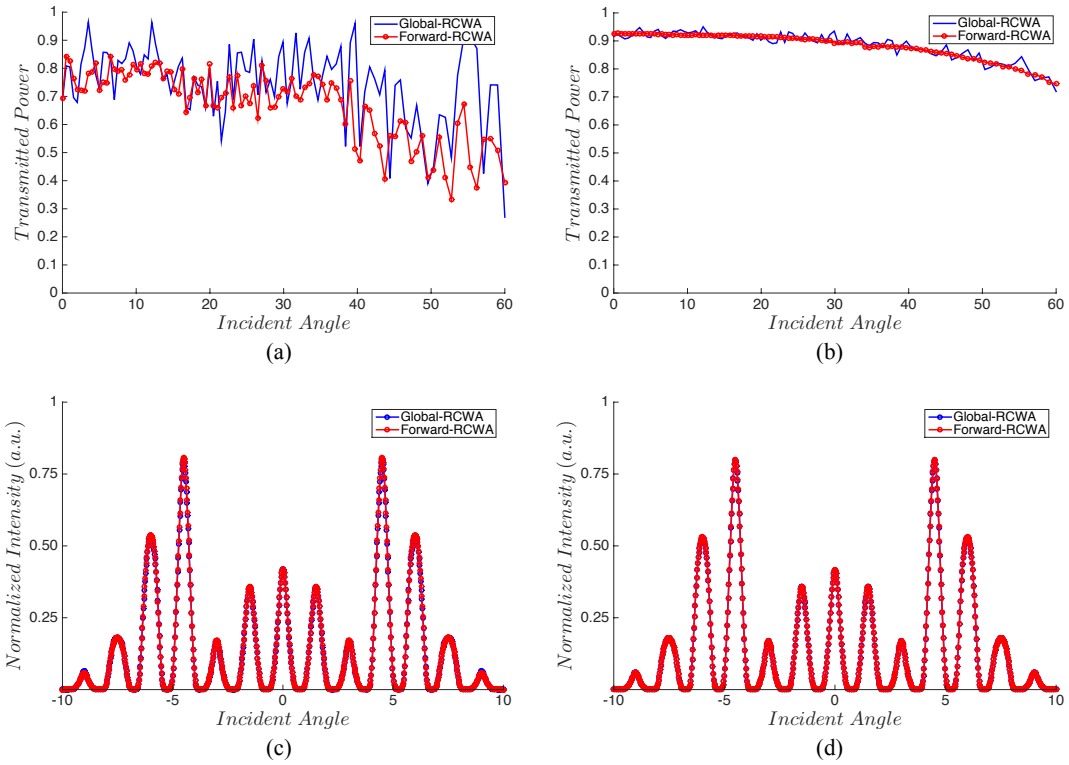

Figure 2-2 Transmitted power calculated through G-RCWA and F-RWA when coupling out to (a) vacuum and (b) index matched material with refractive index 1.6; (c),(d) normalized transmitted intensity corresponding to (a) and (b) respectively.

Bloch waves propagation through the grating. Figure 2-2(b) shows the transmitted power when an index matching oil with refractive index of 1.6 was used in region *II* similar to what was used in the experiment. The index matching oil reduces the amplitude of multiple reflections and the scattering of the field at the output interface. The transmitted beam was also calculated in both non-matched and matched cases as shown in Figure 2-2(c) and Figure 2-2(d), respectively. Although the variations in the transmitted diffraction orders and power are high in the non-matched case, the transmitted intensity profiles are very similar when the sampling is dense enough for both cases. This agreement shows that the F-RCWA approach is sufficiently accurate.

We proceed with the analysis of validity of the semi-analytical approach of Sec. 3.3. The same waveguide parameters were used to analyze the F-RCWA solution using both the proposed semi-analytical and direct DFT approaches. Medium II was chosen to be vacuum. Although the negligible multiple reflections are disregarded in the forward solution, the problem of fast phase variations still exists and requires a large number of samples for the direct solution.

Figure 2-3(a) shows the transmission efficiency of the zeroth diffraction order calculated with F-RCWA. The rapid variations of the individual diffraction orders versus the incident angle are due to the fast phase variations of the propagating Bloch waves. Accurate calculation of the output field would then require a large number of samples in the Fourier domain to be able to follow these rapid variations. However, the phase term $-k_0 q_m d$ and the amplitude term $\tilde{T}_{i,m}$ in Eq. (15) are slowly varying

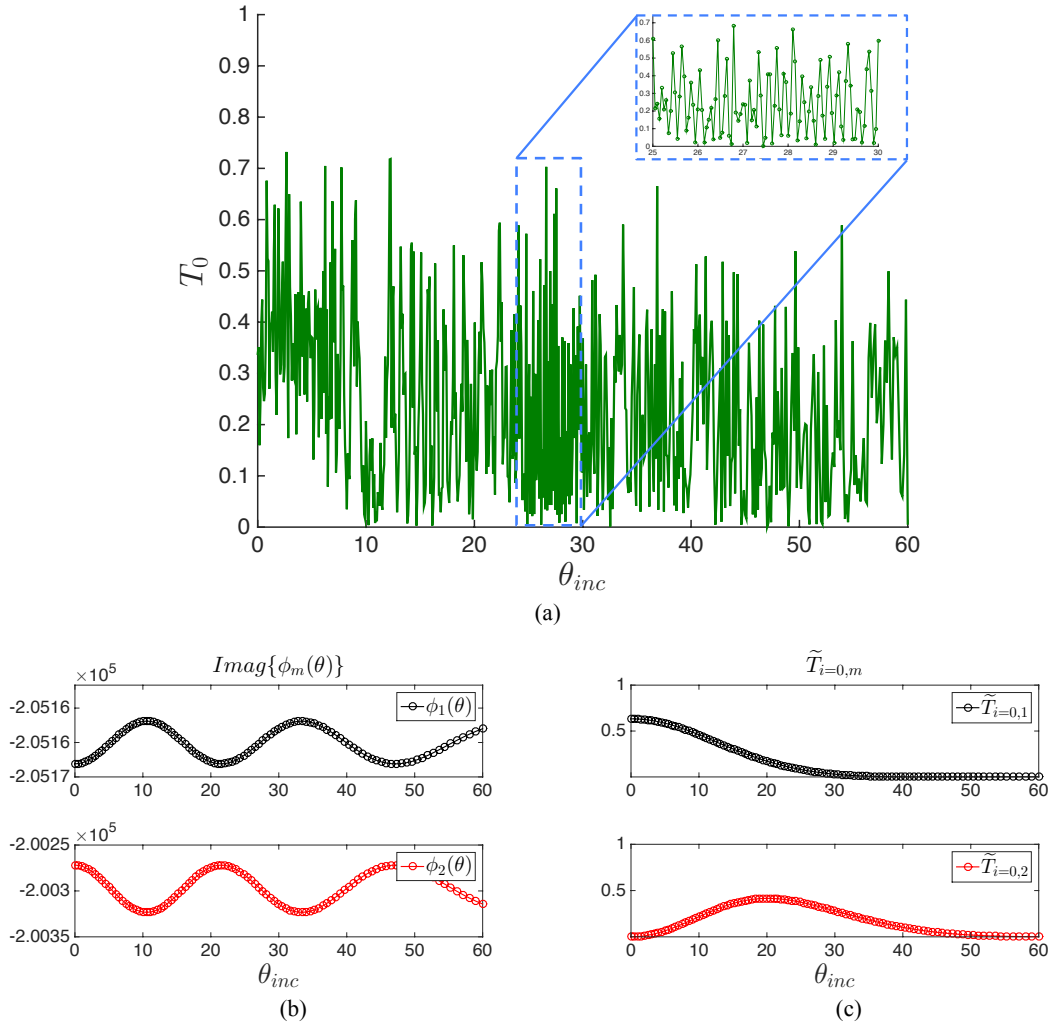

Figure 2-3 Fast variation of 0_{th} diffraction order with incident angle calculated with F-RCWA, (b), (c) slowly varying phase and amplitude as functions of angle.

functions of k_x as seen in Figure 2-3(b) and Figure 2-3(c), which show the phase and amplitude of the first two Bloch waves.

Yet, for a large propagation distance, the exponential summation of the involving phases yields the rapidly varying transmission coefficients as a function of wavenumber (or angle). One can take advantage of the knowledge of these smooth

functions by using Eq. (15) and Eq. (16) to analytically calculate the rapidly varying integrand with much smaller number of samples.

Figure 2-4 compares the semi-analytical and direct FFT approaches using F-RCWA solution as well as the G-RCWA solution for the transmitted output intensity. The same 1 *cm* long waveguide array is considered and the incident wave is a Gaussian beam with a $1/e$ beam radius of $0.8\mu m$ and normal angle of incidence. Medium II was index matched to the refractive index of the fiber core. For this case 2,389 Fourier domain $\left(Mk \right)$ samples are sufficient to represent both the incident field's spectrum and the variations of the Bloch eigenmodes of the waveguide array. This number of samples is enough to calculate the output field properly using the proposed semi-analytical approach of Eq. (17). However, if the conventional direct inverse (FFT) approach is used one has to increase the number of samples in the Fourier domain from 2,389 to 286,515 (a factor of 120 for the given examples) in order to calculate the transmitted field properly. Using the proposed method one can calculate the output field efficiently and accurately with a much smaller (sparser) number of samples compared to the conventional direct inverse FFT method. One can clearly note the excellent matching between the efficient semi-analytic approach with 2,389 points compared to the direct FFT approach with 286,515 points.

In order to quantify the efficiency of the proposed method, Normalized Root Mean Square Error (NRMSE) of the output intensity was calculated versus the depth of the same waveguide array through F-RCWA. The error is defined as

$$NRMSE = \sqrt{\frac{\int_L (I_1 - I_2)^2 \, dx}{\int_L I_1^2 \, dx}} \tag{18}$$

where I_1 is the accurate solution calculated with G-RCWA, I_2 is the solution with semi-analytic and direct F-RCWA methods for smaller number of samples, and L is the integration range. Figure 2-5 shows the calculated normalized RMSE through direct IFFT and the proposed semi-analytic approach. The error is then calculated with respect to the accurate field in the ±10 μm range (i.e. L = 20 μm) for all depths of the waveguide array. As the depth of grating is increased a larger number of samples is required to achieve the same level of accuracy. The reason for that, as described before, is the faster variation of the transmitted diffraction orders and propagating

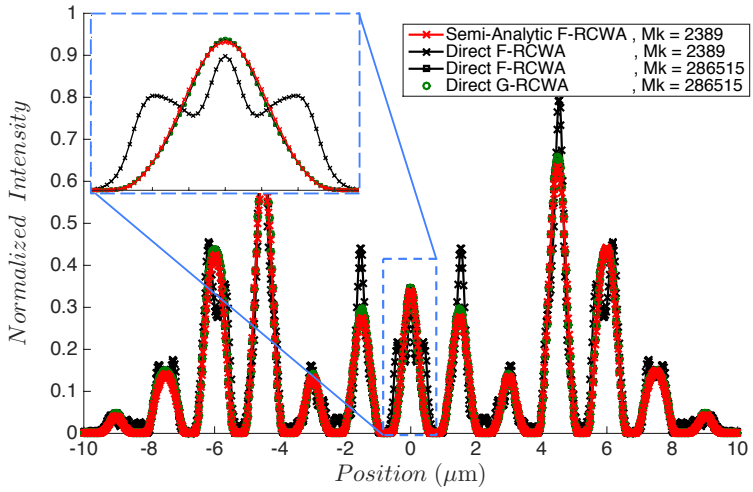

Figure 2-4 Transmitted field after 1cm of propagation through the waveguide array calculated with F-RCWA.

Bloch waves with spatial frequency (angle), which requires a larger number of samples to calculate the field properly. For the same number of samples, the proposed semi-analytic approach yields a more accurate result as it calculates the inverse Fourier transform peace-wise analytically.

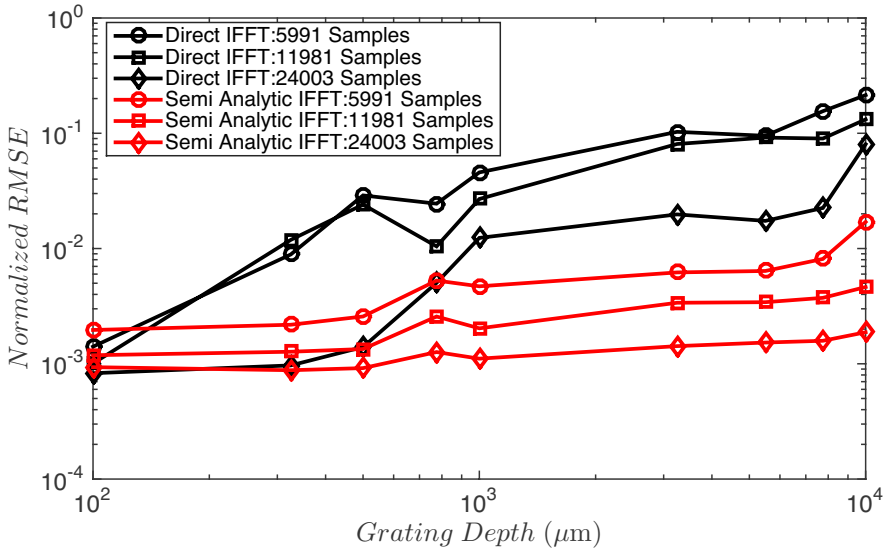

Figure 2-5 Normalized RMSE for F-RCWA calculated with direct IFFT and proposed semi analytic integration.

Importantly, the accuracy of the proposed semi-analytical method is to an acceptable level independent of the depth of grating. Therefore, the electric or magnetic field can be calculated at any depth without the need to increase the number of samples as long as the initial number of samples is high enough to smoothly follow the Bloch waves variations with incident angle. The computation time of the proposed semi-analytic method, direct F-RCWA method and direct G-RCWA method on a single core of a 2.6 GHz Intel Core i7-3720QM CPU is presented in Figure 2-6. The number of samples was chosen such that the normalized RMSE was fixed at the value of 2% for all grating depths by using Eq. (18) for the three calculation methods. One

can note that the computation time for the proposed method is nearly independent of the grating depth. The slight increase of the computational time for deeper gratings in the proposed method is due to the fact that in this case higher order Bloch waves contribute more to the output beam and hence a slightly greater number of samples is required. The proposed method is much faster than both direct G-RCWA and direct F-RCWA methods.

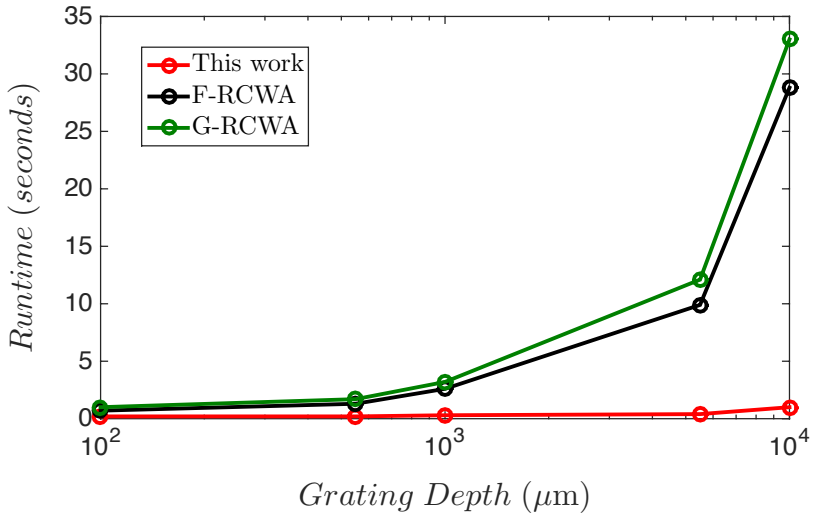

Figure 2-6 Computation time for 2% NRMSE error using this work, F-RCWA and G-RCWA methods

Table 2-1 summarizes the improvement in computation time and number of samples for the given problem. It is evident that the proposed method is up to 33 faster than the G-RCWA and F-RCWA methods for the given grating depths.

Table 2-1 Improvement in computation parameters compared with G-RCWA.

Depth (um)	**100**	**550**	**1000**	**5500**	**10000**
Improvement in Computation Time	5x	8.5x	10.7x	30.2x	33x
Improvement in # of Samples	4.1x	7.5x	8.5x	22x	25.1x

Finally, Figure 2-7 shows the normalized intensity of a 1D periodic waveguide array calculated with the proposed method. The waveguide core and cladding refractive indices are 1.554 and 1.550 and the widths are 3.5 μm and 5 μm respectively. The incident wave is a Gaussian beam with $1/e$ beam width of 3 μm at a wavelength of 633 nm and normal angle of incidence. We note that that the intensity profile at each height was calculated using the same Bloch eigenmodes and eigenvectors. As the Gaussian beam propagates through the waveguide, it couples into the adjacent waveguides and the diffraction pattern of the waveguide array is observed.

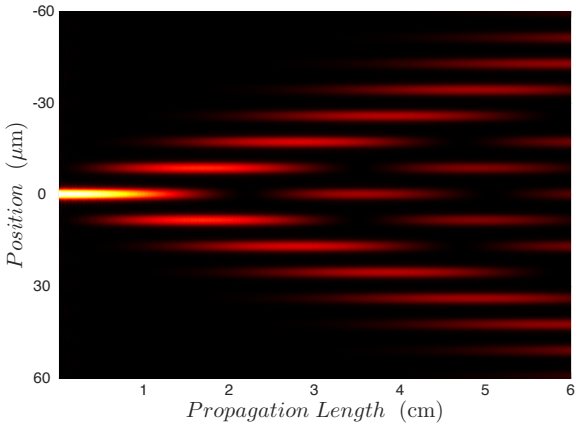

Figure 2-7 Intensity pattern of a 1D periodic waveguide array

2-5 Conclusions

An efficient numerical method was proposed to calculate the transmission of an electromagnetic beam through a deep periodic dielectric grating. The incident beam was decomposed into its Fourier spectrum of plane waves and the propagating Bloch waves for the periodic grating region were calculated for each plane wave component using RCWA. The RCWA solution was simplified by considering the forward propagating contributions and it was shown that there is an insignificant difference between the F-RCWA and G-RCWA solutions for deep gratings. As the depth of grating increases the variation of the transmission coefficients becomes faster as a function of spatial frequency, and therefore a larger number of samples is required for accuracy. Individual treatment of the propagating Bloch waves enabled us to calculate the inverse Fourier transform semi-analytically using both analytical integration of individual Bloch waves and FFT. The advantage was using the FFT to maintain the speed while accounting for the fast phase variations through analytical integration to maintain the accuracy of calculations with a smaller number of samples. It was shown that the presented formulations lead to accurate and efficient calculation of the output field.

Acknowledgements

Chapter 2, in full, is a reprint of the material as it appears in "Efficient analysis of deep high-index-contrast gratings under arbitrary illumination", Motamedi, Nojan; Shlivinski, Amir; Ford , Joseph E.; Lomakin, Vitaliy, *Optics express* 23, no. 26 (2015): 33472-33483. The dissertation author was the primary investigator and author of this paper.

This research was supported by the DARPA SCENICC program under contract W911NF-11-C-0210. The research was conducted while A. Shlivinski was on sabbatical leave at the University of California San Diego. The authors would like to thank Dr. Salman Karbasi for invaluable discussions.

References

[1] O. Coquoz, C. D. Depeursinge, R. Conde, and E. B. de Haller, “Microendoscopic holography with flexible fiber bundle,” Proc. SPIE 2132, 466-474 (1994).

[2] G. Oh, E. Chung, and S. H. Yun, “Optical fibers for high-resolution in vivo microendoscopic fluorescence imaging,” Opt. Fiber Technol. **19**(6), 760-771 (2013).

[3] T. S. Axelrod, N. J. Colella, and A. G. Ledebuhr, "The wide-field-of-view camera," in Energy and Technology Review, (Lawrence Livermore National Laboratory, 1988).

[4] J. Ford, I. Stamenov, S. J. Olivas, G. Schuster, N. Motamedi, I. P. Agurok, R. Stack, A. Johnson, and R. Morrison. "Fiber-coupled monocentric lens imaging," in Imaging and Applied Optics Technical Papers, OSA Technical Digest (Optical Society of America, 2013), paper CW4C.2.

[5] S. Karbasi, A. Arianpour, N. Motamedi, W. M. Mellette, and J. E. Ford, "Quantitative analysis and temperature-induced variations of moiré pattern in fiber-coupled imaging sensors," Appl. Opt. **54**(17), 5444-5452 (2015).

[6] A. Arianpour, N. Motamedi, I. P. Agurok, and J. E. Ford, "Enhanced signal coupling in wide-field fiber-coupled imagers," Opt. Express **23**(4), 5285-5299 (2015).

[7] K. L. Reichenbach and C. Xu, "Numerical analysis of light propagation in image fibers or coherent fiber bundles," Opt. Express **15**(5), 2151-2165 (2007).

[8] X. Chen, K. L. Reichenbach, and C. Xu, "Experimental and theoretical analysis of core-to-core coupling on fiber bundle imaging," Opt. Express **16**(26), 21598-21607 (2008).

[9] J.-H. Han and J. Kang, "Effect of multimodal coupling in imaging micro-endoscopic fiber bundle on optical coherence tomography," Appl. Phys. B **106**(3), 635–643 (2012).

[10] F. Montiel, and M. Neviere, "Differential theory of gratings: extension to deep gratings of arbitrary profile and permittivity through the R-matrix propagation algorithm," J. Opt. Soc. Am. A **11**(12), 3241-3250 (1994).

[11] K. Knop, "Rigorous diffraction theory for transmission phase gratings with deep rectangular grooves," J. Opt. Soc. Am. **68**(9), 1206-1210 (1978).

[12] T. Delort, and D. Maystre, "Finite-element method for gratings," J. Opt. Soc. Am. A **10**(12), 2592-2601 (1993).

[13] T. Iizuka, and C. M. de Sterke, "Corrections to coupled mode theory for deep gratings," Phy. Rev. E **61**(4), 4491-4499 (2000).

[14] D. Marcuse, Light Transmission Optics (Van Nostrand Reinhold, 1972).

[15] A. Yariv, "Coupled-mode theory for guided-wave optics," IEEE J. Quantum Electron. **9**(9), 919-933 (1973).

[16] S.-D. Wu, T. K. Gaylord, E. N. Glytsis, and Y.-M. Wu , "Three-dimensional converging-diverging Gaussian beam diffraction by a volume grating," J. Opt. Soc. Am. A **22**(7), 1293-1303 (2005).

[17] M. G. Moharam, E. B. Grann, D. A. Pommet, and T. K. Gaylord, "Formulation for stable and efficient implementation of the rigorous coupled-wave analysis of binary gratings," J. Opt. Soc. Am. A **12**(5), 1068-1076 (1995).

[18] M. G. Moharam, D. A. Pommet, E. B. Grann, and T. K. Gaylord, "Stable implementation of the rigorous coupled-wave analysis for surface-relief gratings: enhanced transmittance matrix approach," J. Opt. Soc. Am. A **12**(5), 1077-1086 (1995).

[19] "An Introduction to Fiber Optic Imaging" download available at http://www.us.schott.com/lightingimaging/english/download/fo.book.pdf.

[20] N. Motamedi, S. Karbasi, J. E. Ford, and V. Lomakin, "Analysis and characterization of high-resolution and high-aspect-ratio imaging fiber bundles," Appl. Opt. **54**(32), 9422-9431(2015).

Chapter 3 Analysis of 3D Straight Fiber Bundles

3-1 Introduction

High-contrast imaging Fiber Bundles (FB) are characterized and modeled for wide-angle and high-resolution imaging applications. Scanning Electron Microscope (SEM) images of fiber bundles cross-section are taken to measure physical parameters and verify the variations of irregular fibers due to the fabrication process. Modal analysis tools are developed that include irregularities in the fiber core shapes and provide results in agreement with experimental measurements. The modeling demonstrates that the irregular fibers significantly outperform a perfectly regular "ideal" array. Using this method, fiber bundles are designed that can provide high contrast with core pitches of only a few wavelengths of the guided light. Structural

modifications of the commercially available fiber bundle can reduce the core pitch by 60% for higher resolution image relay.

Imagers with curved focal planes have been shown to be superior in terms of performance compared to the conventional planar focal plane imagers due to the lower aberration and simpler design with fewer number of optical elements [1]. Realization of curved focal planes is however challenging due to the fabrication difficulties associated with non-planar surfaces. Although different groups have successfully demonstrated curved focal planes [2-4] and stretchable electronics [5-7] have been known as a potential solution to the challenging problem of curved focal plane fabrication, they either have large radius of curvature or more importantly have low resolution. Little attention has been paid to the curved image sensors and the characteristics of the curved focal planes are far from the flat image sensors. Alternatively imaging fiber bundles can be shaped into a curved focal plane using micro grinding. Imaging Fiber Bundles have been used in numerous applications including illumination, tomography and endoscopy [8-11]. Recently high-resolution imaging FBs have been used for compact wide-angle and high-resolution imaging applications [12-14] where the curved image plane is mapped onto the flat sensor-plane or a secondary flat image-plane using the FBs. The motivation of using FBs is to make the conventional imagers more robust and compact by taking advantage of monocentric lenses with curved image planes. Figure 3-1(a) shows the fiber-coupled imager's cross-section cut along the fiber length. Image captured by the monocentric lens is formed on the curved side of FB. The image is then relayed to the image sensor

through the straight FB. Modeling, characterization, and optimization of these straight fiber bundles have gained interest for integrated imaging applications. Tapered and non-straight imaging FBs have also been used in the fiber-coupled imagers to achieve better system integration [15]. The focus of this work is on straight fiber bundles. Figure 3-1(b) shows the SEM image of the fiber-coupled imager's cross-section showing the FB along with the image sensor.

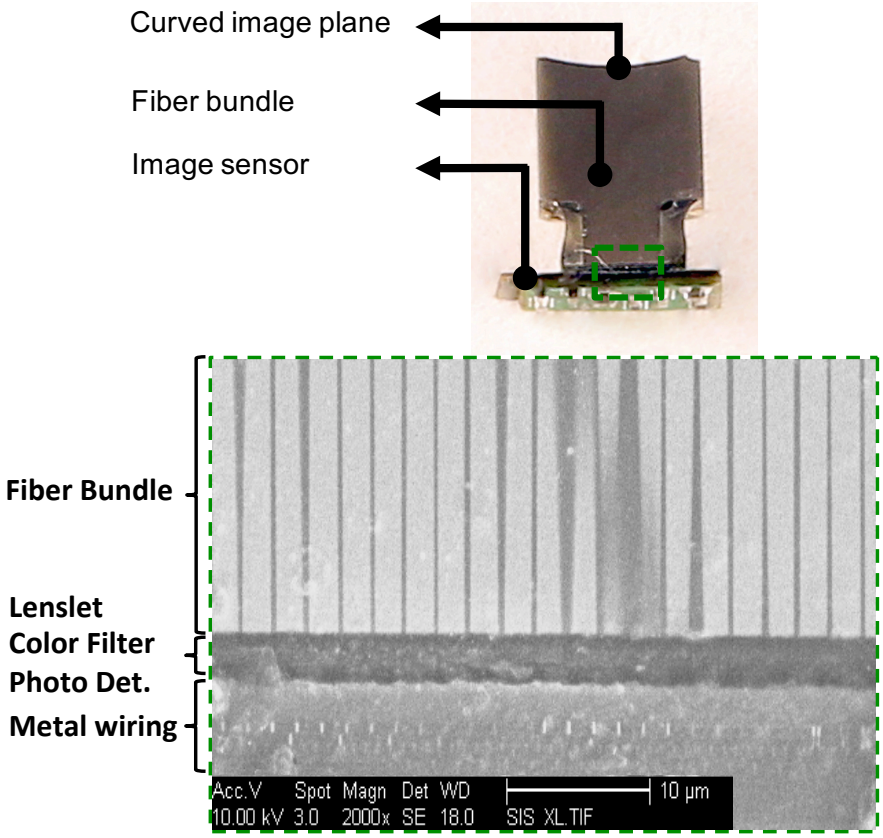

Figure 3-1 (a) Fiber-coupled image sensor cut along the fibers and (b) its SEM cross-section.

Fiber coupled imagers resolution is limited by the FB pitch, as state of the art image sensors are able to oversample and resolve individual fibers. Furthermore, in order to avoid the moiré pattern associated with fiber coupled imagers [16] proper

design of finer FBs is required. Finer pitches of FB may be fabricated by tapering them further. However, the performance of FBs in terms of transmitting an image with a low cross-talk at a fixed wavelength would also diminish. Poor impulse response of the FB would result in image blur and decreases the image resolution in this type of imagers.

A set of straight FBs with different spatial resolutions (pitch) varying from 2.5 μm to 1.0 μm are characterized experimentally by placing them on a USAF resolution chart and evaluating the transmitted image using broadband illumination. Impulse response measurements are also taken by focusing a coherent 612 nm laser light onto the core of a 2.5 μm fiber bundle under various angles of incidence to evaluate the light confinement.

Modal analysis has been used to analyze the core-to-core coupling of imaging fibers [17,18] for a lower index contrast fiber bundles (Δn: 0.05). The effect of disorder was studied in [17] for fiber bundles with 3.2 μm and 4.5 μm pitches using coupled mode theory and by considering only the fundamental mode of the fibers. In this paper, entire guided modes of a 5x5 regular array of fibers are calculated numerically for a higher index contrast (Δn: 0.33) and finer pitches (1.5 μm) of fiber bundle. A Gaussian beam is propagated through the fiber bundle by calculating the overlap integral of incident field and each guided mode. The effect of number of calculated modes and number of fibers in the simulation window is studied for more efficient modeling. An engineered irregularity is then introduced into the model to analyze its effect on the confinement of guided modes and impulse response of fiber

bundle. Mode width diameter is calculated for each guided mode in both regular and irregular fiber bundles to demonstrate higher confinement of irregular fibers. The modified model is then used to improve the performance of the fiber bundles for higher spatial resolutions. SEM cross-section image of the FB is introduced into the model to evaluate the performance of the actual fiber bundle for various pitches.

3-2 Imaging Fiber Bundles

Various pitches of FBs may be fabricated by tapering and drawing them from an initially larger pitch. Fabrication process starts by drawing an individual fiber up to a certain width, cutting and stacking the individual drawn fibers, and redrawing them again. This process is repeated until desired length and pitch of the fiber bundle is reached. Schott's imaging FBs [19] are used throughout this paper for qualitative and quantitative analysis. Figure 3-2(a) shows the scaling of 10 mm long FBs with pitches from 2.5 μm to 1.0 μm. While the number of fibers does not change in each FB, its diameter decreases with the pitch. Schematic of fiber bundle cross-section, as shown in Figure 3-2(b), consists of a high index core, cladding, and extramural absorber material with real part refractive indices of 1.81, 1.48, and 1.54, respectively. The extramural absorber material is used for partial elimination of the background noise associated with radiation modes and cross talk between the fibers. Figure 3-2(c) is the optical microscope image of the 2.5 μm pitch fiber bundle. Extramural absorber material cannot be differentiated from cladding due to a lower refractive index contrast between the cladding and absorber.

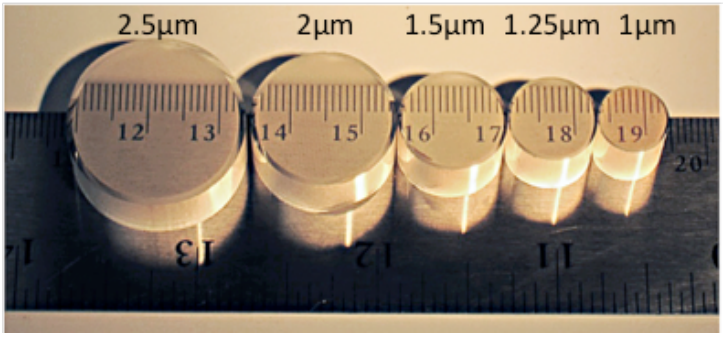

(a)

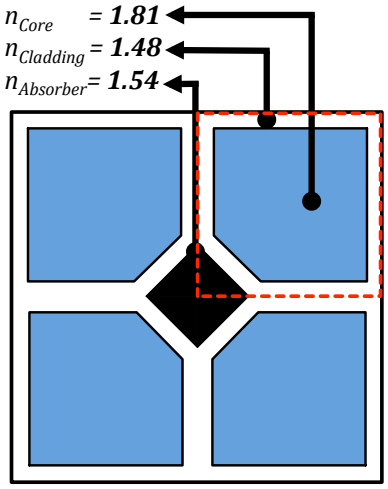

(b)

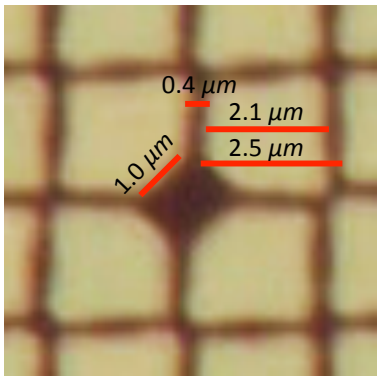

(c)

Figure 3-2 (a) Scaling of imaging fiber bundles with different pitches. (b) Schematic of the 5-sided FB cross-section. (c) 76X-magnification optical microscope image of the FB

Figures Figure 3-3(a) and Figure 3-3(b) show the Scanning Electron Microscope (SEM) image of Schott's FB cross-section with 2.5 µm pitch at 5000x and 15000x magnification. An SEM image of 1.0 µm pitch fiber bundle's cross-section was taken at 5000x and 12500x for comparison. Scaling and physical structure of the 1.0 µm pitch fiber bundle with 2.5x higher magnification [Figure 3-3(d)] is similar to that of the 2.5 µm pitch fiber bundle.

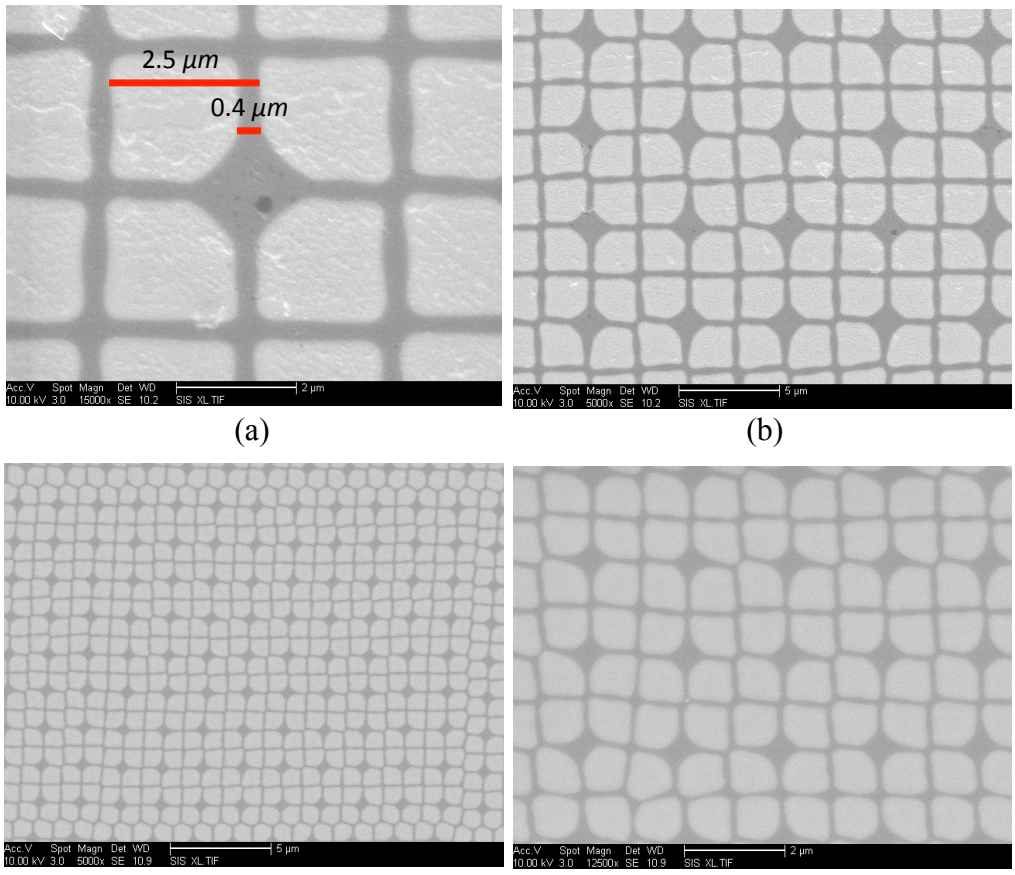

Figure 3-3 (a), (b) SEM image of 5-sided FB with a pitch of at 15,000x and 5,000x magnifications; (c), (d) pitch of at 5,000x and 12,500x magnifications.

SEM images of various pitches of fiber bundles were converted to black and white images [Figure 3-4(a)] for measurement and modeling purposes. The 2.5 μm and 1.0 μm pitch fiber bundles of Figure 3-2(a) were used for taking SEM data. The core area (white regions) percentage with respect to the total area of FB's cross section was measured as a metric to ensure that the FB's structure is preserved for the 2.5 μm and 1.0 μm pitches. Three different SEM images were taken for each bundle pitch and the average core area was measured to be 69.3% and 69.1% for the 2.5 μm and 1.0 μm bundles, respectively. The measured core area percentages verify insignificant

variation during the drawing process. The 69.1% and 69.3% core areas are close to the nominal core area of FB and are referred as 70% core area in the rest of the paper.

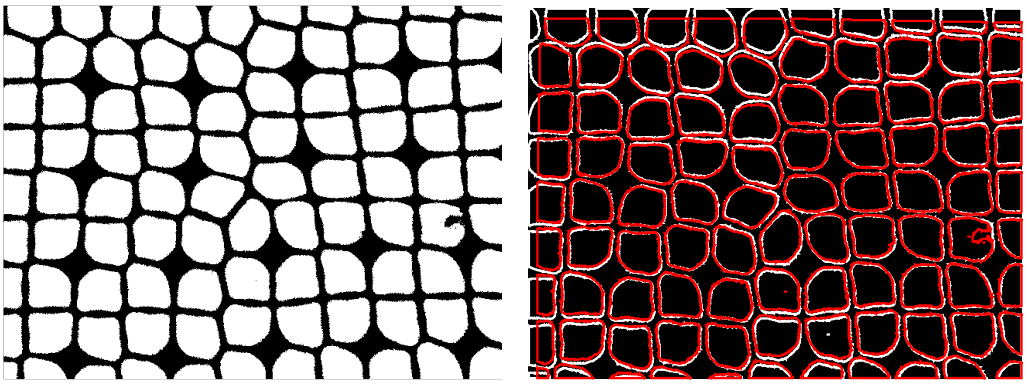

(a) (b)

Figure 3-4 (a) Conversion of SEM image to black (cladding and absorber regions) and white (core region). (b) Core boundaries obtained from the SEM image of 5-sided FB with a pitch of $2.5\mu m$ (White boundaries from side 1 and red boundaries from side 2 after 10mm fiber drawing).

In order to ensure that FB preserves its structure i.e. the core and cladding's shape, width and scaling, an SEM image of a particular irregular area was taken from both input and output facets of a 10 mm long fiber bundle. Core boundaries locations of the fiber bundle were extracted from the black and white image of the FB cross-section at both facets. Otsu's thresholding method [20] was used to extract the black and white (binary) image from the gray scale SEM image. The boundaries of black and white regions were registered as core boundaries. The core boundaries of both facets were then superimposed for comparison. Because the image of the output facet is a mirrored image of the same area on the input facet of FB, one of the SEM images also has to be flipped in order to be directly comparable. Figure 3-4(b) shows the superimposed images of the FB's core boundaries. The flipped image of the core boundaries from the output facet (red lines) coincides well with the core boundaries

from input facet (white lines) after 10 mm of fiber bundle drawing with negligible variation in the size, shape and location of individual fibers. This also validates the assumption of straight fiber bundle for modeling purposes.

3-3 Characterization of FB

Three types of measurements are taken for qualitative and quantitative characterization of fiber bundles. Different pitches of fiber bundles are placed on top of a resolution chart with bottom wide-angle white light illumination. The cross talk of transmitted images is compared. Then a 612 nm He-Ne laser is focused on the center of a 2.5 μm fiber bundle and the output intensity profile is recorded for different angles of incidence. Finally, a collimated white light source is used to assess the cross-talk width in various pitches of fiber bundles and for different angles of incidence.

3-3-1 Qualitative Characterization

Fiber bundles with various pitches were placed on top of a USAF resolution chart as shown in Figure 3-5. An index matching oil with refractive index of 1.6 was used between the FB and resolution chart to minimize scattering of light and the gap between resolution chart and fiber bundles.

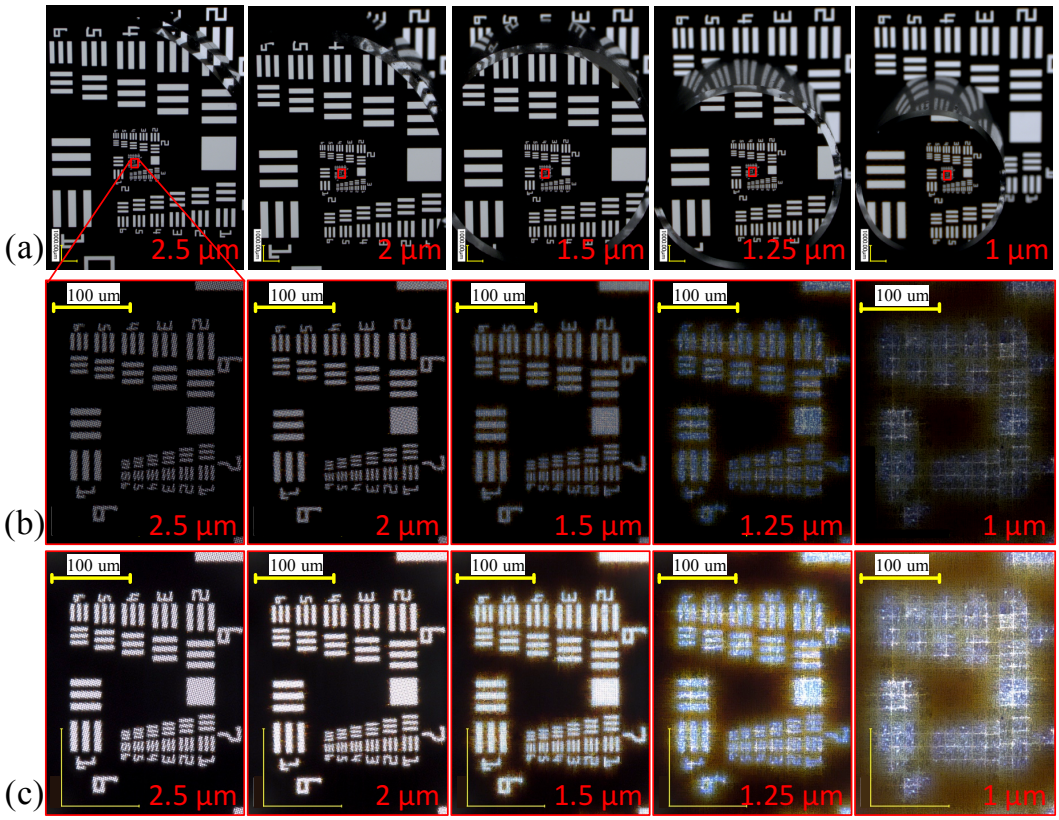

Figure 3-5 Qualitative examination of scaling effect on the performance of FBs, (a) different pitches of fiber bundles on top of the resolution chart, (b) 20X magnification image passed through the 1cm long FB, (c) the same image as in (b) but saturated to magnify the cross-talk between the fiber cores.

Figure 3-5(a) shows different pitches of the FBs ranging from 1.0 µm to 2.5 µm. As described in the previous section, finer pitches are fabricated by drawing the same array of fibers and they all have the same 10 mm length. Figure 3-5(b) shows the 20x magnification image from the finest set of bars on the resolution chart under the same lighting conditions. The numerical aperture of the capturing microscope (Keyence VHX-1000) for this experiment was 0.48 with working distance of 25 mm. The width of one line in the six elements of groups 6 and 7 on the resolution chart varies from 7.81 µm to 4.38 µm and 3.91 µm to 2.19 µm, respectively. A partially collimated white light was used for all pitches. The individual fibers may be seen in

the 2.5 μm, 2.0 μm and even the 1.5 μm pitch fiber bundles. Finer pitches of FBs are ideal for imaging applications if each individual fiber maintains the spatial properties of the image with minimized cross talk between adjacent fibers. However, scaling down the bundle pitch would lead to a thinner cladding width at a fixed wavelength. Since the field decays exponentially outside the core region, a thinner cladding at a fixed wavelength would lead to a stronger field at the core-cladding interface of the adjacent fibers, thus increasing the cross-talk between individual fibers. This explains why the 1.25 μm and 1.0 μm fibers do not maintain the same image quality as larger fiber pitches. Similar results were observed with higher numerical aperture objective (NA 0.9) and the lower confinement of fiber bundles at finer pitches will be confirmed in our quantitative experiment in section 3-3-3. Figure 3-5(c) shows the saturated image in the same region as in Figure 3-5(b), where the exposure time was increased so that the aforementioned cross-talk is more visible.

3-3-2 Quantitative Characterization, Impulse Response

FBs are shift-variant optical elements and therefore the linear shift-invariant (LSI) analysis cannot be applied. However, the optical impulse response measurements can give us an intuition about the performance of the fiber bundles for

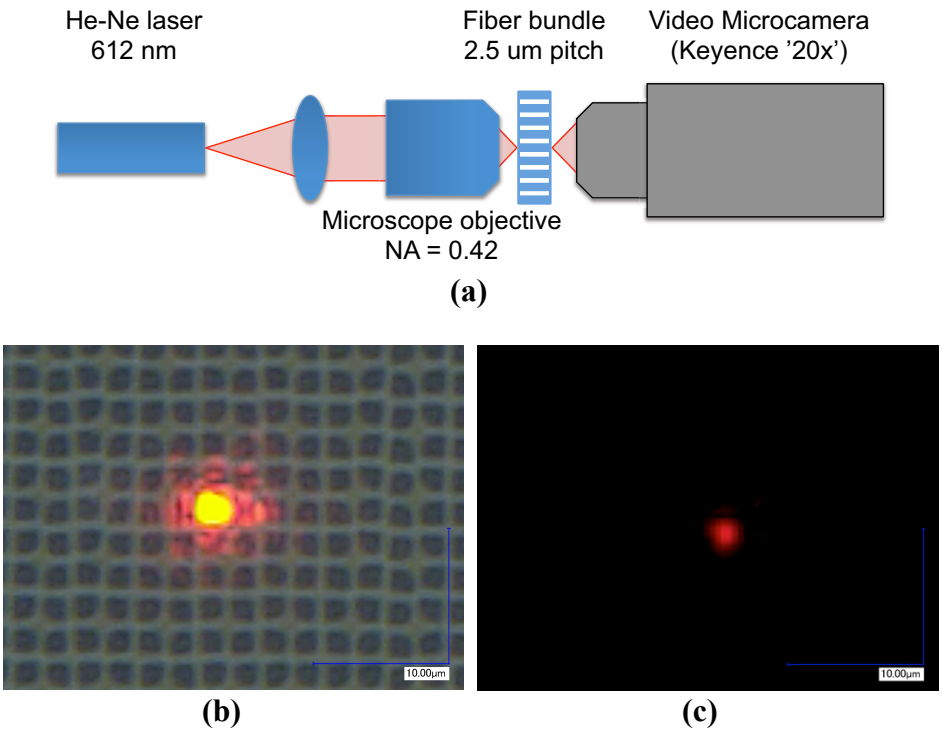

Figure 3-6 (a) Schematic of impulse response measurement, (b) saturated focused laser light with white light background to illuminate the fiber grid, and (c) focused laser light on the center of the fiber core.

image-transmitting applications. The transmission of a 2.5 µm pitch fiber bundle was measured by focusing a collimated He-Ne laser on the core of fiber bundle using a microscope objective with numerical aperture (NA) of 0.42. The transmitted image was then captured using an optical microscope with NA of 0.48 on the other side of fiber bundle. The He-Ne laser operated at a wavelength of 612 nm. The measured spot size (airy disk diameter) of the launched beam was 2.1 µm which is close to the theoretical diffraction-limited spot size of the microscope objective (1.8 µm). Figure 3-6(b) shows the saturated image of the focused laser light on the center of a fiber core with a white-light background to show the fiber bundle grid. The intensity profile of the beam in the back end of the fiber bundle in Figure 3-6(c) shows no cross-talk to

the adjacent cores. The fiber bundle was then tilted for illumination at larger angles of incidence.

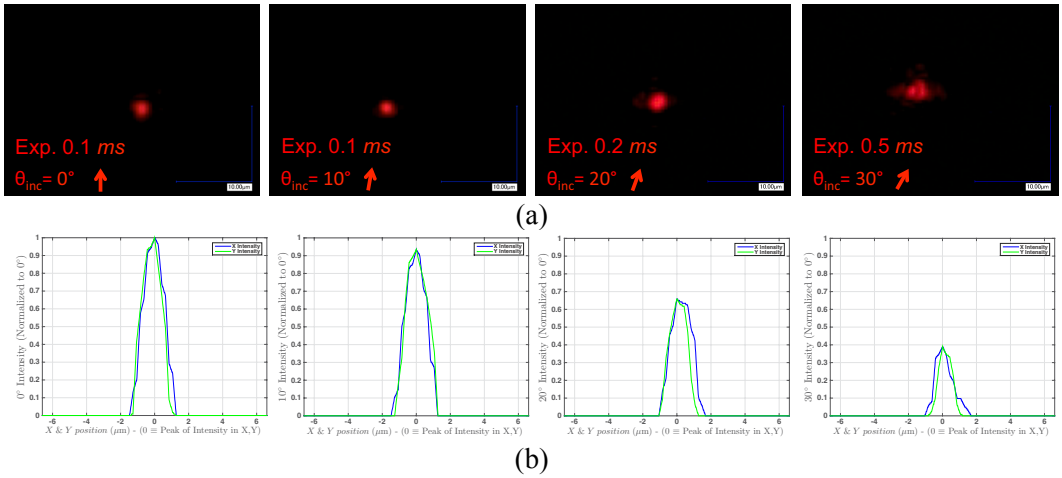

Figure 3-7 Impulse response measurement at different angles of incidence, (a) 2D output intensity profile and (b) normalized X (blue) and Y (green) intensity cross-section centered at peak.

Figure 3-7 shows the fiber bundle's transmitted image for different angles of incidence. The exposure time was increased from 0.1 ms to 0.5 ms for larger angles of incidence. Figure 3-7(b) is the corresponding X and Y plot of intensity for each angle of incidence with the center being the peak intensity. All figures are normalized by considering the exposure times and peak-intensity values. As the angle of incidence increases the transmitted intensity and power decreases due to low input and output coupling of light from the fiber bundle. Limited numerical aperture of the capturing objective would decrease the accuracy of calculations at larger angles of incidence. Because of the diffraction limit (1.8 μm) of the focusing objective, finer pitches of fiber bundles cannot be characterized using this measurement technique. Moreover FBs are highly shift-variant optical elements, such that the measurement setup is highly sensitive to vibrations and the results could not be regenerated reliably.

Although this type of measurement demonstrates the confinement of 2.5 μm pitch fiber bundle an alternative measurement technique is required to characterize the cross-talk of fiber bundles at finer pitches.

3-3-3 Quantitative Characterization, Slant-Edge Measurement

For more quantitative characterization of cross-talk in the fiber bundles an alternative measurement technique was used. The schematic of measurement setup is shown in Figure 3-8(a), where a bright white led light source was placed against a 500 μm pinhole. An achromat lens was then placed at the distance equivalent to the lens focal length to create a collimated white light. The white led light source was used in order to measure the average cross-talk value for all visible wavelengths as opposed to single wavelength characterization. FBs were placed on top of USAF resolution chart and were illuminated by the collimated white light at three angles of incidence: 0°, 22.5° and 45°. A high numerical aperture objective with NA of 0.9 was used to capture the transmitted image off the output surface of fiber bundles. Figure 3-8(b) shows the transmitted image of an edge through a 10 mm long fiber bundle with a pitch of 2.5 μm at normal incidence. In order to be able to measure the cross-talk between individual fibers, the transmitted light was examined near the edge. Cross talk was quantified by first averaging the intensity of the transmitted image in the direction

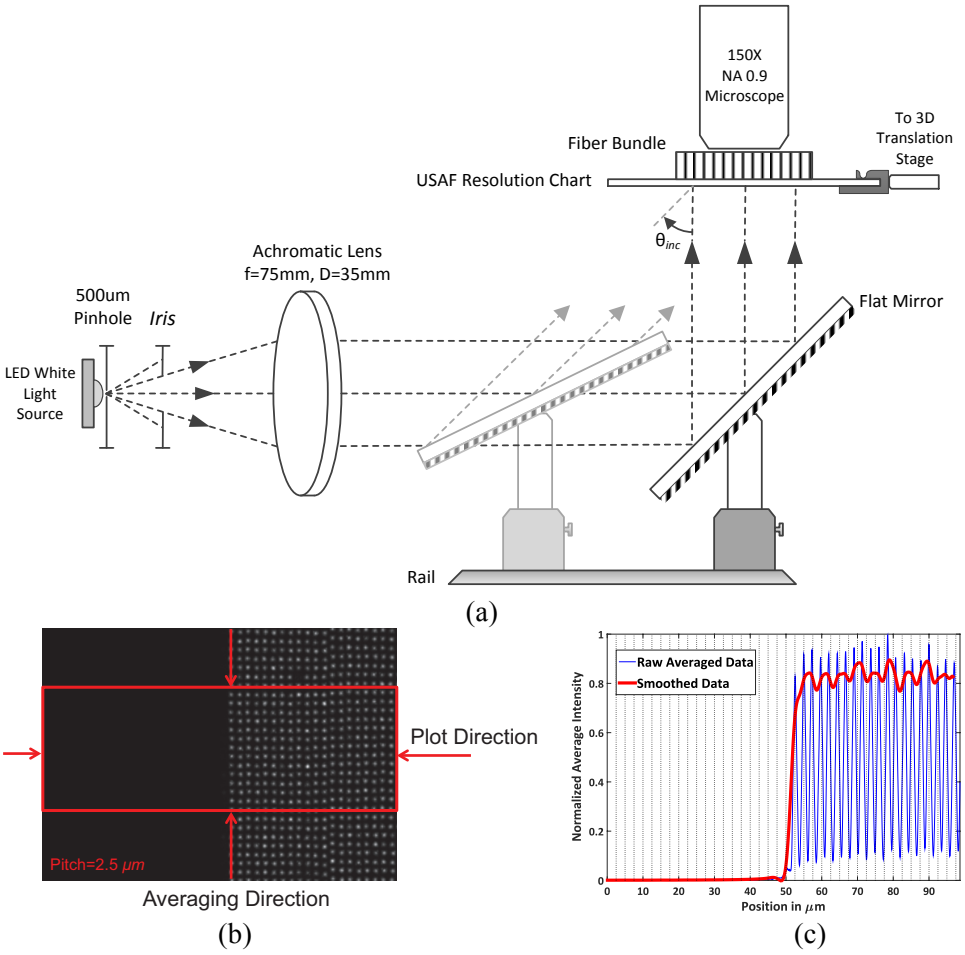

Figure 3-8 Schematics of the measurement setup: collimated white light incident on the FB on top of USAF resolution chart, (b) transmitted image of the edge through the FB at normal incidence, (c) averaged intensity plot in the direction normal to the edge.

parallel to the edge over 500 pixels in the image which is equivalent to physical length of 33 μm. This would compensate for fiber bundle's defects and random variations in size and location as well as the intensity variations of the collimated light source. The averaged intensity was then plotted in the direction normal to the edge [Figure 3-8(c)]. What appears in the background of the raw averaged data in blue curve is in fact the effect of misalignment of fibers in each column (parallel to the edge) and the intensity fluctuation within each fiber.

A smoothing spline curve fitting [21] was applied to the averaged data to get a smoother transition from the bright to dark region (red curve) as well as eliminating the intensity fluctuations between fiber bundles due to their shift-variant property. The smoothing parameter was chosen such that the transition is smooth for calculating the intensity transition width from 80% to 10% of the peak. The same smoothing parameter (10^{-4}) was chosen to smoothen all measured data consistently. The cross-talk width varies depending on the value of smoothing parameter but the consistency of measurements is preserved for a constant value of smoothing parameter. This metric was used for measuring the cross-talk between individual fibers at all pitches.

It is important to characterize the FBs for different angles of incidence in imaging applications, where a conventional lens is used to focus a cone of light on the image plane, which in this case is the FB's input facet. Figure 3-9(a) shows the transmitted image off a 10 mm long fiber bundle with 2.5 μm pitch at three different angles.

All of the images were taken under the same lighting conditions but the exposure time was increased from 3.2 s to 16 s for higher angles of incidence. The intensity plots were normalized to the intensity of normal incidence image. At normal incidence, the overlap between the incident field and the lowest order modes of the individual fibers are high. As a result, the transmitted light through each fiber bundle appears as a combination of the first few lower-order modes. Since the lower-order modes of a multimode fiber are more confined, the transmitted light intensity is also

higher at the center of the core and decays rapidly as it gets off the center. This would make the fiber bundle strongly shift variant at normal incidence. In the experimentally demonstrated fiber-coupled imager [12] the transmitted image of the fiber will be sampled directly by an image sensor, which is shift variant itself. Therefore in the cases where FB's pitch is comparable with the image sensor pitch a moiré pattern will be observed [16,22-24]. It has been shown that the moiré pattern can be reduced by proper image processing [16,22-24].

As the angle of incidence increases, higher-order modes of the fibers are excited as well as the lower-order modes. Since higher-order modes are less confined the transmitted light through the fiber bundle would be less shift-variant. The transmitted intensity and power decreases by increasing the angle of incidence due to lower coupling into and from the fiber bundle. The absorber material also reduces the

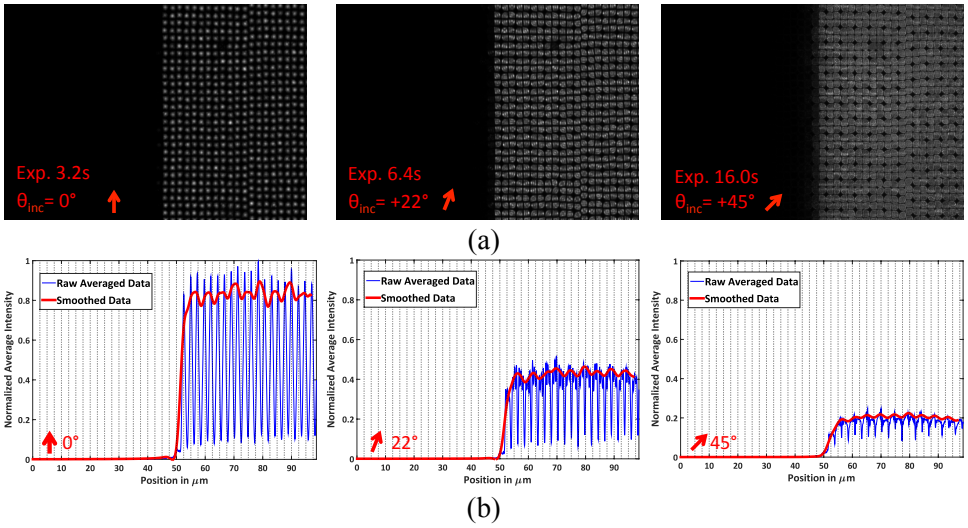

Figure 3-9 (a) Transmitted image through 2.5 μm pitch fiber bundle at different angles of incidence and (b) their average intensity plot in the direction normal to the edge.

transmitted power due to stronger field in the absorber at higher angles of incidence. These measurements are in agreement with the impulse response measurement. However, the slant edge measurement can be repeated reliably and for all pitches, and therefore it is a more suitable experiment for fiber bundle characterization. Figure Figure 3-9(b) shows the intensity plot of the transmitted image of the edge through the fiber bundle in the direction normal to the edge for three different angles of incidence.

Table 3-1 Cross talk width (μm) of different pitches of FBs for various incident angles

$Pitch / \theta_{inc}$	-45°	-22°	0°	22°	45°
1 μm	53.9	28.2	23.7	29.9	52.3
1.25 μm	29.2	21.2	21.8	20.7	33.9
1.5 μm	18.8	10.1	5.1	11.7	21.4
2 μm	16.4	4.7	2.5	6	13
2.5 μm	5.5	3.9	2.1	3.8	5.1

Table 3-1 shows the cross-talk width of different pitches of FBs for different angles of incidence. Due to shift-variant property of the fiber bundles and smoothing curve fitting that was applied to the measured intensity, the measured cross-talk width is larger than the fiber pitch. The cross-talk width consistently increases for greater angles of incidence and finer pitches of fiber bundle. The positive and negative angles of incidence show the same degree of cross-talk, but the cross-talk width is highly affected by the fiber bundle pitch. As the fiber bundle pitch decreases at the same wavelength, the decaying field in the cladding region gets stronger at the core-

cladding interface of the adjacent fiber leading to stronger cross-talk between fibers after a certain threshold is reached. The measured cross-talk is in agreement with the qualitative measurements presented in section 3-A, where in both cases the finer pitches of the fiber bundles show poor performance. In order to improve the performance of FBs at finer pitches one has to either increase the refractive index contrast between the core and cladding [25], which raises fabrication complications, or increase the cladding thickness to further suppress the field decay in the cladding region. The details of performance improvement of the FBs are discussed in the subsequent section.

3-4 Modeling of Imaging Fiber Bundles

The pitch of fiber bundles varies from 1.0 μm to 2.5 μm (~ 2-5 λ) while the length is on the order of millimeters (~ 10^4 λ). Full-scale rigorous modeling of the FBs is, therefore, extremely hard due to the large aspect ratio and overall size. Although two-dimensional modeling of fiber bundles [26,27] (1D periodicity + propagation) provides an intuition of the scaling effect and cross-talk, it may be inaccurate for quantitative 3D modeling of realistic fiber bundles. Here we use an approach in which the modes of a finite size array of waveguides are calculated using the cross section of the actual fiber bundles. This is achieved by introducing the SEM cross-section images of the FB into the model. The overlap integral between the incident beam and each of the guided modes is calculated to get the coupling coefficients. These coefficients are then used to calculate the transmitted beam at any length.

3-4-1 Formulation

The transmitted field at a desired propagation length inside the fiber bundle can be computed via modal superposition:

$$E_T(x,y,z) \approx \sum_m c_m E_m(x,y) e^{-jk_0 n_{eff,m} z} \tag{3-1}$$

where $E_m(x,y)$ is the m^{th} electric field mode profile of the fiber bundle, $n_{eff,m}$ is the m_{th} mode effective index ($k_0 n_{eff,m}$ is the corresponding modal wavenumber), and c_m is the coupling coefficient to the m^{th} mode. The modes are global in the sense that they include the coupling between all the (finite number of) fibers considered in the model. The summation in Eq. (1) is taken over the guided modes considering that for the long-range propagation studied here, the modal cross-talk is dominated by the coupling between the guided modes, while all radiation/leaky modes are scattered out and are diminishing at the output plane.

The guided modes of the fiber bundle can be found numerically using a Finite Element Method (FEM) or Finite Difference Method. Here, the modes are found via FEM. The modal coefficients c_m are found by approximating the field at the incidence plane by the incident field, which assumes that the coupling of the incident beam into the fiber bundle is strong. This assumption is justified by the fact that we can often use a matching material. Additionally, a complete 2D (1D cross-section) analysis demonstrates that the propagation confinement results obtained with and without this assumption are similar. To this end, the incident field is expanded as [28]:

$$E_{inc} = \sum_m c_m E_m(x,y) \tag{3-2}$$

One can further multiply both sides of Eq. (3-2) by the complex conjugate of the nth magnetic field mode profile H_n^* and integrate the resulted power:

$$\iint \left(E_{inc} \times H_n^* \right).e_z \, dx\, dy = \iint \left(\sum_m c_m E_m \times H_n^* \right).e_z \, dx\, dy \tag{3-3}$$

where e_z is the unit vector in the propagation direction z. Using the mode orthogonality, the coefficients of the overlap integral can be written as:

$$c_m = \frac{\iint \left(E_{inc} \times H_m^* \right).e_z \, dx\, dy}{\iint \left(E_m \times H_m^* \right).e_z \, dx\, dy} \tag{3-4}$$

The integrals in Eq. (3) are calculated numerically based on the FEM solutions for the modes. With the coefficients in Eq. (3), the transmitted field is found via Eq. (1).

3-4-2 Analysis of Computation Parameters

Modal analysis of high contrast fiber bundles may be time consuming and the computation time scales quadratically with the number of fibers. Therefore, proper choice of the number of calculated modes and the number of fibers kept in the computation domain is important. Depending on the illumination angular spectrum a lower number of modes may be used to calculate the propagated beam.

Root Mean Square Error (RMSE) of normalized intensity of a 1.5 μm pitch fiber bundle after 0.5 mm propagation was calculated with different number of modes in a 5x5 array of fibers with 70% core area. RMSE was calculated from the following:

$$RMSE = \sqrt{\iint \left(I_{exact} - I_{apr.} \right)} \tag{3-5}$$

where I_{exact} is the exact normalized output intensity calculated using all the guided modes and $I_{apr.}$ is the normalized output intensity calculated using fewer number of guided modes approximation. The incident field is a Gaussian beam with a radius of 0.5 μm at a wavelength of 612 nm. The input Gaussian beam radius was chosen such that it mostly excites a single fiber at the input facet of the fiber bundle even for tilted inputs. The cross-talk observed at the output is then strictly due to the coupling between fibers during propagation of light. For larger beam width, the coupling to the adjacent cores may occur because of the input coupling. Propagation length of 0.5 mm is long enough for observing the cross-talk in the 1.5 μm pitch fiber array.

Figure 3-10(a) shows the RMS error versus the number of modes for various angles of incidence. Small variation in the RMS error for smaller angles of incidence indicates that a smaller number of modes may be calculated for these cases. As the angle of incidence increases a larger number of modes is required to achieve the same error. Figure 3-10(b) and Figure 3-10(c) show the transmitted beam at a distance of 0.5 mm for a normally incident Gaussian beam calculated with all (678) guided modes and with only the lowest 3 guided modes; a good agreement is obtained between these cases. On the other hand for the 30 degrees of incidence case [Figure 3-10(d) and

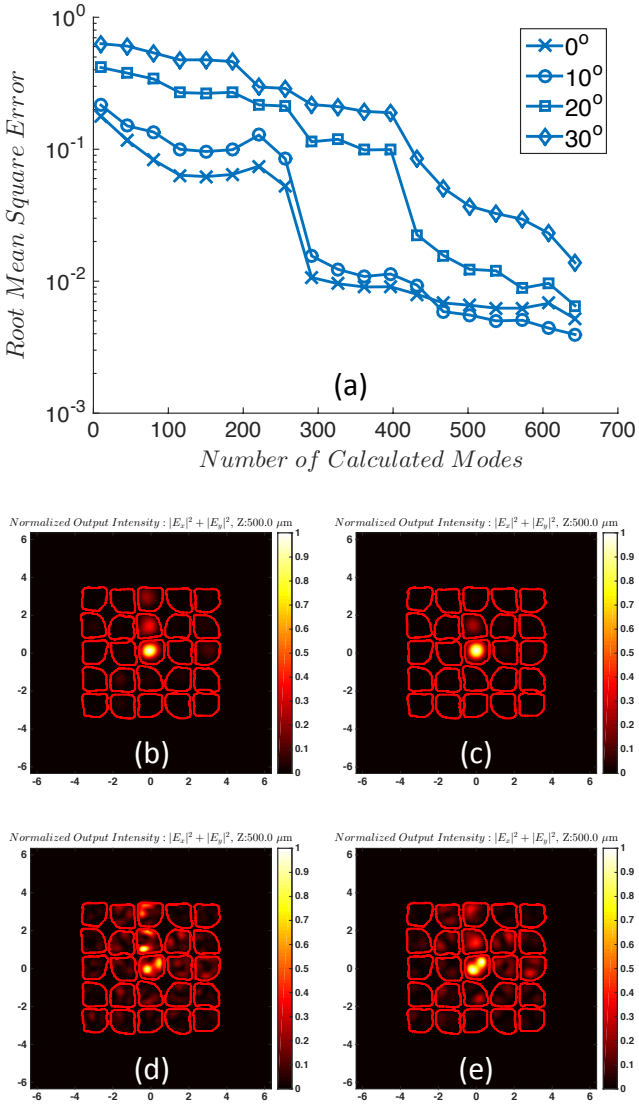

Figure 3-10 RMSE for 5x5 array of fibers with 70% core area with 1.5 μm pitch, impact of number of calculated modes kept in calculations for different angles of incidence. (a) RMS error vs. the number of modes; (b) the transmitted field for normal incidence with all of the 678 modes and (c) with only 3 modes; (d) the transmitted field for *30°* incidence with all the modes and (e) with 169 modes.

Figure 3-10(e)], a good agreement is obtained only with a larger number (169) of modes. Therefore, fewer number of modes may be calculated depending on the launching condition and parameters of the fiber bundle.

Furthermore, to verify the effects of the number of fibers on the results, a larger array of fibers was modeled using the same modeling method. The binary image of 70% core area fiber bundle (from SEM measurement) was numerically eroded to 50% core area using the methods described in [29,30]. Figure 3-11(a) and Figure 3-11(b) show a 9x9 array of the 1.5 μm pitch FB at the propagation distance of 0.5 mm for 70% and 50% core areas. The 70% core area FB shows a significant cross-talk and the intensity distributions of arrays with a different number of fibers differ due to the large field spread and finite size of the computational domain. On the other hand the intensity distribution of the well-confined 50% core area fiber bundle is identical to that of the 5x5 array. One should note that as far as imaging applications are concerned, a confined impulse response is the most important characteristic of an imaging FB. Once the impulse response is not confined within one fiber, the image detected by the image sensor is blurred and the intensity distribution of the cross-talk is less important. The number of guided modes scales up with the number of fibers and the run time scales up quadratically with the number of fibers. As long as the confinement of fibers is the goal of modeling, a smaller number of fibers and modes may be calculated for modeling depending on the illumination conditions. In the following numerical analysis we used 5x5 arrays to assess confinement and kept the number of included modes sufficiently large for accurate results.

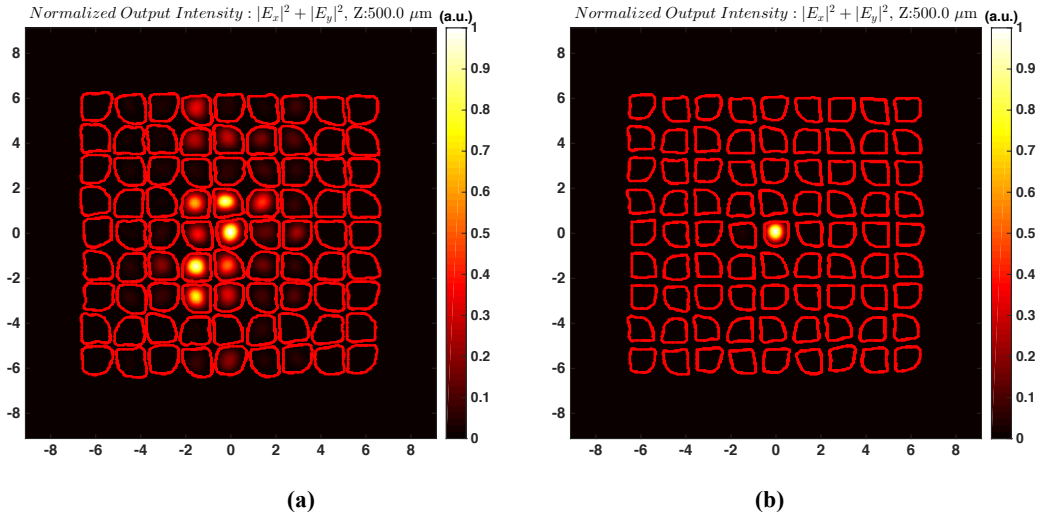

(a) **(b)**

Figure 3-11 Impulse response of a 9x9 array of fibers with $1.5\mu m$ itch for (a) 70% core area and (b) 50% core area.

3-4-3 Introducing Irregularity in the Model

Due to lower refractive index contrast between core and extramural absorber, the actual size of the absorber material cannot be measured from the SEM image and the absorber material was excluded from the model. The modes of the waveguide array were calculated at a wavelength of 612 nm. Figure 3-12(a) shows the transmitted beam intensity from a perfectly regular 1.5 μm pitch waveguide array with core width of 84% fiber pitch after 500 μm propagation. Red five-sided geometries represent the fiber bundle core boundaries and the background material is the same as fiber's cladding. The incident field is a Gaussian beam with beam radius of 0.5 μm and wavelength of 612 nm launched into the central fiber at [0,0].

Transmitted beam is not confined in the launched core due to thinner cladding width at the fixed wavelength, which makes the decay of field weaker, thus increasing

the cross-talk between the fibers. Moreover, perfectly identical fiber cores have a relatively weak confinement due to the strong coupling between them. The effect of fiber bundle disorder was then studied to show that it would significantly increase the field confinement [31]. In order to accurately model imaging fiber bundles effects of disorder were verified numerically by introducing an irregular array of fibers. Each of the fibers core width in the 2x2 fiber array [Figure 3-2(b)] were reduced by 1% of the largest (original) core width in the clockwise direction starting from the upper left fiber. The rest of the fibers in the array were repeated from this disordered 2x2 array. Starting from the upper left fiber, the core widths are 84%, 83%, 82% and 81% of the pitch respectively.

Figure 3-12(b) shows the transmitted intensity in the irregular fiber array. Because the central core width is different from its neighbors, the coupling to these fibers is also weaker, which leads to a lower cross-talk.

The mode width (σ) of each guided mode is calculated for the entire modes of both regular and irregular fiber bundles using second moment method [32]:

$$\sigma^2 = \int_{-\infty}^{+\infty} (x - x_0)^2 I(x,y)\, dx\, dy \tag{3-6}$$

where x_0 is the center of the mode:

$$x_0 = \int_{-\infty}^{+\infty} x I(x,y)\, dx\, dy \tag{3-7}$$

Figure 3-12(c) and Figure 3-12(d) show the mode width count versus mode width for both the regular and irregular fiber bundles. All of the guided modes in the

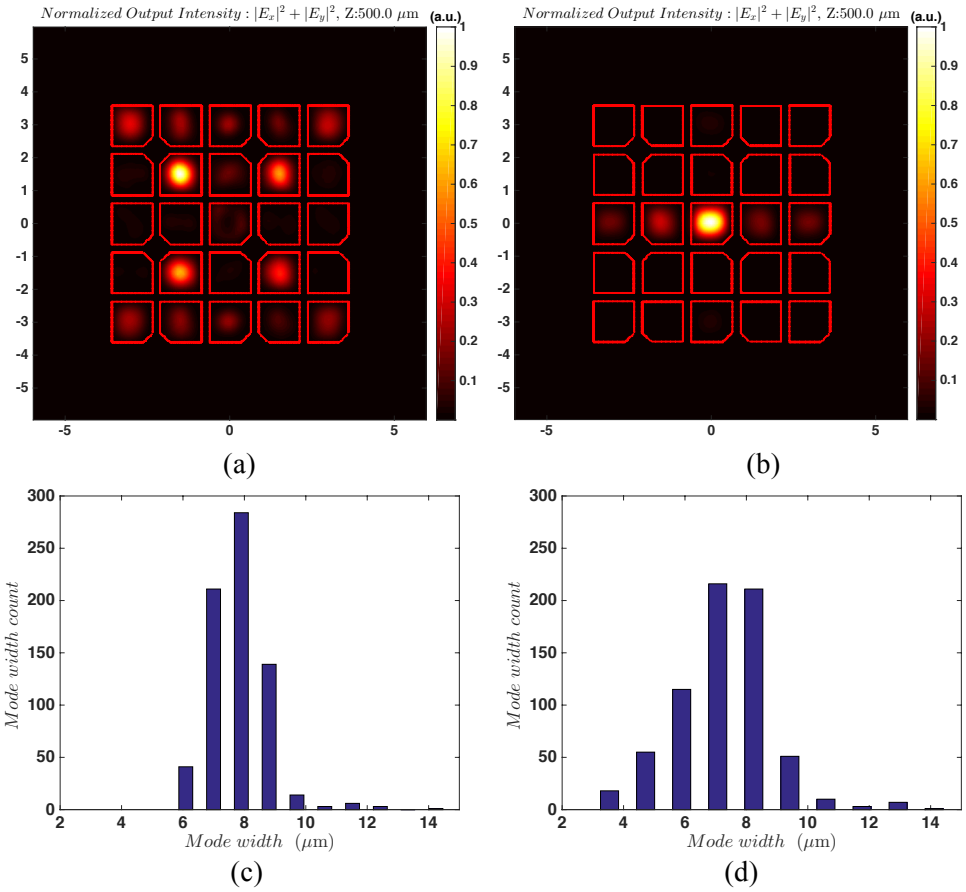

Figure 3-12 Impulse response of a 9x9 array of fibers with $1.5\mu m$ itch for (a) 70% core area and (b) 50% core area.

regular fiber bundle have widths greater than 6 µm while in the irregular fiber bundle the modes (33 count) have widths as low as 3.5 µm. Therefore, it is evident that introducing fabrication or engineered irregularities into fiber bundle is crucial for proper modeling and higher confinement.

3-4-4 Modeling and Improvement of the Actual FB Cross-Section

An SEM image of the 2.5 μm pitch fiber bundle cross-section [Figure 3-3(b)] was used to model the performance of an actual fiber bundle. Figure 3-13(a) shows the corresponding normalized transmitted intensity. The transmitted beam is well confined

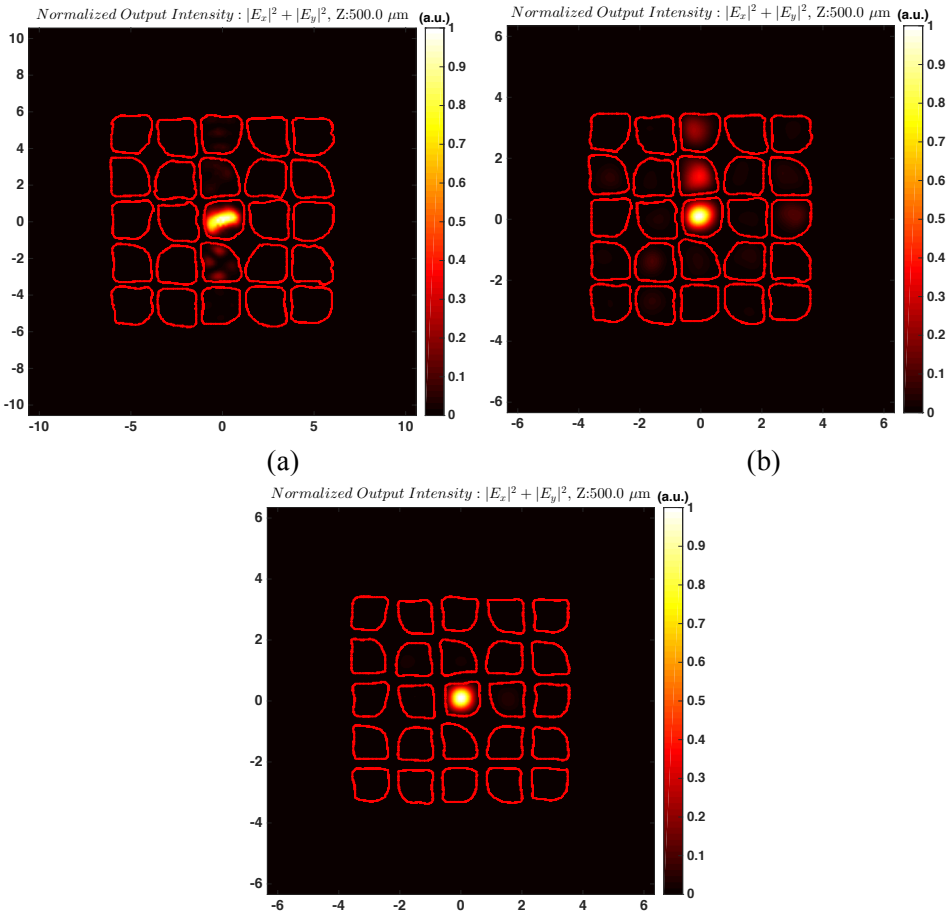

Figure 3-13 Normalized transmitted intensity in (a) SEM cross section of 2.5 μm pitch fiber bundle with 70% core area, (b) same scaled cross section used for 1.5 μm pitch and (c) numerically eroded to 50% core area with 1.5 μm pitch.

within the launching core and it is in agreement with the measurement in Figure 3-6(c). The fibers irregularity associated with FB fabrication process improves the performance of fiber bundles in terms of cross-talk. However, when the same fiber bundle structure is scaled down from 2.5 μm pitch to 1.5 μm the irregularity is not sufficient to get the same confined optical impulse response.

Instead, the modes of each fiber are more extended along the cladding leading to a higher cross-talk between fibers as seen in Figure 3-13(b). One way to overcome this limitation is to increase the core-cladding refractive index contrast. However, increasing the refractive index contrast further would introduce fabrication challenges.

An alternative way to increase the FB resolution is increasing the cladding thickness so that modal field becomes weaker across the cladding, thus reducing the cross-talk. In order to verify this point, the same fiber array of Figure 3-13(b) was numerically eroded from 70% to 50% core area. Figure 3-13(c) shows the normåalized transmitted intensity of the 1.5 μm pitch fiber bundle with a 50% core area. The impulse response of the 1.5 μm pitch fiber bundle is well confined within the launch core. Therefore, a higher resolution in a fiber bundle may be achieved by increasing the cladding, at the cost of loosing the light collection and increasing shift-variance of the FBs.

Angled illumination of the 2.5 μm pitch and 5 mm long fiber bundle with the same structure also shows high confinement as shown numerically and experimentally in Figure 3-14(a) and Figure 3-14(b), respectively.

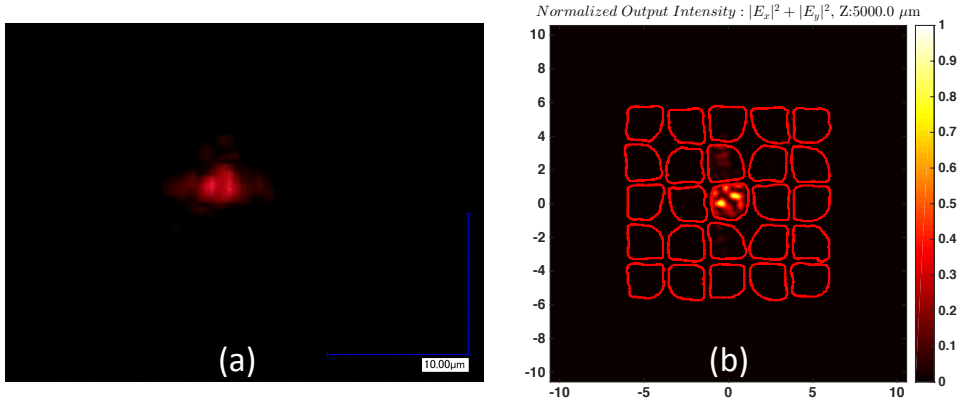

Figure 3-14 Comparison of normalized intensity of (a) measured intensity and (b) the numerical model of the 2.5 μm pitch fiber bundle for 30° angle of incidence after 5 mm propagation.

3-5 Conclusions

High resolutions imaging FBs were characterized using coherent and incoherent excitations. The characterization included both measurement and numerical simulation. The measurements consisted of qualitative analysis of the image transported through different pitches of FBs, impulse response characterization of a 2.5 μm pitch fiber bundle and finally quantitative analysis of the cross-talk with incoherent collimated white light illumination.

Modal analysis was used to model the extremely deep FBs. The numerical investigation shows a relatively small number of modes and guiding cores can be used for efficient modeling of the fiber bundles as a guide for fabrication of high resolution imaging fiber bundles. As the fiber bundle's pitch scales down from 2.5 μm to 1.0 μm the performance of FBs gets worse at the same wavelength. This is explained by a lower confinement and larger extension of guided modes into cladding. This effect

limits the resolution of the commercially available fiber bundle with *NA = 1* to 2.5 μm. We proposed increasing the resolution of the fiber bundle by reducing the fill fraction of the fiber cores. Introducing disorder into the fiber bundle was shown to be crucial for improving the confinement and image resolution. One has to note that fabrication-induced disorder should be differentiated from engineered disorder. An engineered disorder may be introduced by simply choosing the initial fibers to have different core areas before the drawing process. Although the uncontrolled fabrication-induced disorder randomly varies the final shape of these fibers, the engineered disorder preserves its nature as the core area of individual fibers remains constant. Optimization of imaging fiber bundles using engineered and uncontrolled disorder is the topic of further investigation.

Acknowledgements

Chapter 3, in full, is a reprint of the material as it appears in "Analysis and characterization of high-resolution and high-aspect-ratio imaging fiber bundles", Motamedi, Nojan; Karbasi, Salman; Ford , Joseph E.; Lomakin, Vitaliy, *Applied optics* 54, no. 32 (2015): 9422-9431. The dissertation author was the primary investigator and author of this paper.

This research was supported by the DARPA SCENICC program under contract W911NF-11-C-0210.

References

[1] S.-B. Rim, P. B. Catrysse, R. Dinyari, K. Huang, and P. Peumans, "The optical advantages of curved focal plane arrays," Opt. Express 16, 4965-4971 (2008).

[2] H.-C. Jin, J. R. Abelson, M. K. Erhardt, and R. G. Nuzzo, "Soft lithographic fabrication of an image sensor array on a curved substrate," J. Vac. Sci. Technol. B 22, 2548-2551 (2004).

[3] R. Dinyari, S.-B. Rim, K. Huang, P. B. Catrysse, and P. Peumans, "Curving monolithic silicon for nonplanar focal plane array applications," Appl. Phys. Lett. 92, 091114 (2008).

[4] D. Dumas, M. Fendler, F. Berger, B. Cloix, C. Pornin, N. Baier, G. Druart, J. Primot, and E. le Coarer, "Infrared camera based on a curved retina," Opt. Lett. 37, 653-655 (2012).

[5] H. C. Ko, M. P. Stoykovich, J. Song, V. Malyarchuk, W. M. Choi, C.-J. Yu, J. B. Geddes Iii, J. Xiao, S. Wang, Y. Huang, and J. A. Rogers, "A hemispherical electronic eye camera based on compressible silicon optoelectronics," Nature 454, 748-753 (2008).

[6] I. Jung, G. Shin, V. Malyarchuk, J. S. Ha, and J. A. Rogers, "Paraboloid electronic eye cameras using deformable arrays of photodetectors in hexagonal mesh layouts," Applied Physics Letters 96, 021110 (2010).

[7] Y. M. Song, Y. Xie, V. Malyarchuk, J. Xiao, I. Jung, K.-J. Choi, Z. Liu, H. Park, C. Lu, R.-H. Kim, R. Li, K. B. Crozier, Y. Huang, and J. A. Rogers, "Digital cameras with designs inspired by the arthropod eye," Nature 497, 95-99 (2013).

[8] T. Xie, D. Mukai, S. Guo, M. Brenner, and Z. Chen, "Fiber-optic-bundle-based optical coherence tomography," Opt. Lett. 30, 1803-1805 (2005).

[9] C. Liang, K.-B. Sung, R. R. Richards-Kortum, and M. R. Descour, "Design of a high-numerical-aperture miniature microscope objective for an endoscopic fiber confocal reflectance microscope," Appl. Opt. 41, 4603-4610 (2002).

[10] G. Oh, E. Chung, and S. H. Yun, "Optical fibers for high-resolution in vivo microendoscopic fluorescence imaging," Opt. Fiber Technol. 19, 760-771 (2013).

[11] T. S. Axelrod, N. J. Colella, and A. G. Ledebuhr, "The wide-field-of-view camera," Energy and Technology Review, 1-12 (1988).

[12] J. Ford, I. Stamenov, S. J. Olivas, G. Schuster, N. Motamedi, I. P. Agurok, R. Stack, A. Johnson, and R. Morrison, "Fiber-coupled Monocentric Lens Imaging," in Imaging and Applied Optics, OSA Technical Digest (online) (Optical Society of America, 2013), CW4C.2.

[13] I. Stamenov, A. Arianpour, S. J. Olivas, I. P. Agurok, A. R. Johnson, R. A. Stack, R. L. Morrison, and J. E. Ford, "Panoramic monocentric imaging using fiber-coupled focal planes," Opt. Express 22, 31708-31721 (2014).

[14] A. Arianpour, N. Motamedi, I. P. Agurok, and J. E. Ford, "Enhanced signal coupling in wide-field fiber-coupled imagers," Opt. Express 23, 5285-5299 (2015).

[15] J. E. Ford, I. Stamenov, S. Karbasi, A. Arianpour, N. Motamedi, I. Agurok, R. Stack, A. Johnson, R. Morrison, J. Mott, E. Martin, C. LaReau, B. Giffel, J. Pessin, R. Tennill, and P. Onorato, "Panoramic Imaging Via Curved Fiber Bundles," in Imaging and Applied Optics 2015, OSA Technical Digest (online) (Optical Society of America, 2015), ITh1A.4.

[16] S. Karbasi, A. Arianpour, N. Motamedi, W. M. Mellette, and J. E. Ford, "Quantitative analysis and temperature-induced variations of moiré; pattern in fiber-coupled imaging sensors," Appl. Opt. 54, 5444-5452 (2015).

[17] K. L. Reichenbach and C. Xu, "Numerical analysis of light propagation in image fibers or coherent fiber bundles," Opt. Express 15, 2151-2165 (2007).

[18] J. H. Han and J. U. Kang, "Effect of multimodal coupling in imaging micro-endoscopic fiber bundle on optical coherence tomography," Appl. Phys. B 106, 635-643 (2012).

[19] "An Introduction to Fiber Optic Imaging," download available at http://www.us.schott.com/lightingimaging/english/download/fo.book.pdf.

[20] N. Otsu, "A threshold selection method from gray-level histograms," Automatica **11**, 23-27 (1975).

[21] C. Reinsch, "Smoothing by spline functions," Numer. Math. **10**, 177-183 (1967).

[22] S. J. Olivas, N. Nikzad, I. Stamenov, A. Arianpour, G. Schuster, N. Motamedi, W. M. Mellette, R. A. Stack, A. R. Johnson, R. Morrison, I. Agurok, and J. E. Ford, "Fiber Bundle Image Relay for Monocentric Lenses," in Classical Optics 2014, OSA Technical Digest (online) (Optical Society of America, 2014), CTh1C.5.

[23] S. J. Olivas, M. Šorel, A. Arianpour, I. Stamenov, N. Nikzad, G. M. Schuster, N. Motamedi, W. M. Mellette, R. A. Stack, A. Johnson, R. Morrison, I. P. Agurok,

and J. E. Ford, "Digital image processing for wide-angle highly spatially variant imagers," in 2014), 91930B-91930B-91911.

[24] S. J. Olivas, A. Arianpour, I. Stamenov, R. Morrison, R. A. Stack, A. R. Johnson, I. P. Agurok, and J. E. Ford, "Image processing for cameras with fiber bundle image relay," Appl. Opt. 54, 1124-1137 (2015).

[25] X. Chen, K. L. Reichenbach, and C. Xu, "Experimental and theoretical analysis of core-to-core coupling on fiber bundle imaging," Opt. Express 16, 21598-21607 (2008).

[26] N. Motamedi, A. Shlivinski, J. E. Ford, and V. Lomakin, "Efficient analysis of deep high-index-contrast gratings under arbitrary illumination," Opt. Exp. 23, 33472-33483 (2015).

[27] S.-D. Wu, T. K. Gaylord, E. N. Glytsis, and Y.-M. Wu, "Three-dimensional converging–diverging Gaussian beam diffraction by a volume grating," J. Opt. Soc. Am. A 22, 1293-1303 (2005).

[28] D. Marcuse, "Loss Analysis of Single-Mode Fiber Splices," Bell System Technical Journal 56, 703-718 (1977).

[29] R. van den Boomgaard and R. van Balen, "Methods for fast morphological image transforms using bitmapped binary images," CVGIP: Graphical Models and Image Processing **54**, 252-258 (1992).

[30] R. Adams, "Radial Decomposition of Disks and Spheres," CVGIP: Graphical Models and Image Processing **55**, 325-332 (1993).

[31] S. Karbasi, K. W. Koch, and A. Mafi, "Modal perspective on the transverse Anderson localization of light in disordered optical lattices," J. Opt. Soc. Am. B 30, 1452-1461 (2013).

[32] A. E. E. D. D. M. Siegman, "How to (Maybe) Measure Laser Beam Quality," in DPSS (Diode Pumped Solid State) Lasers: Applications and Issues, OSA Trends in Optics and Photonics (Optical Society of America, 1998), MQ1.

Chapter 4 Image Restoration in Fiber-Coupled Imagers

4-1 Introduction

Fiber coupled image sensors are capable of high-resolution conformal image transfer, including mapping of the spherical image surface of a monocentric wide-angle lens to one or more flat focal plane sensors. However, image resolution is lost due to fiber bundle defects, moiré from lateral fiber-sensor misalignment, and blur due to the non-zero gap between fiber bundle and the image sensor. In this chapter we investigate whether sub-pixel impulse response characterization of the strongly shift-variant impulse response can be used with existing image processing techniques to recover the resolution otherwise lost in image transfer. We show that the sub-micron

impulse response is experimentally repeatable, and can be used to recover image data and reveal fine features of the input surface structure of a 2.5 μm pitch fiber bundle.

Some optical systems require a non-planar image sensor, which is incompatible with the high-performance (large pixel count, low noise and sensitivity) focal planes fabricated with conventional CMOS processing. One example is the curved image surface formed by a wide-field "monocentric" lens [1], which requires a far deeper curvature than can be achieved by elastic deformation of a continuous CMOS focal plane die [2], and requires more spatial resolution than can be achieved with a spatially segmented CMOS sensor structure [3]. However, optical fiber bundles (a dense array of small, high index contrast multimode fiber cores with low index contrast cladding) can transfer the image from the curved focal plane to the flat image sensor plane [1,4]. A fiber-coupled (FC) image sensor consists of a quasi-periodic fiber bundle (created by glass stretching, stacking, and re-stretching) bonded directly to the face of a perfectly periodic image sensor. The fiber pitch is typically around 2.5 μm, and with appropriate design may be reduced to 2 μm or less [5,6]. The input field of view in a fiber-coupled monocentric lens imager achievable with a spherical-planar fiber bundle can be increased from approximately 50˚ with a single straight fiber bundle, to over 124˚ with a single tapered fiber bundle, where the fibers are curved towards the spherical input surface [7]. However, the high spatial resolution of the fiber bundles can be significantly reduced due to light transmission across any gap between the planar surface of the fiber bundle and the image sensor. This gap is typically several microns, which is comparable to the fiber pitch. Fiber defects and

micron-size particles also appear as artifacts in the captured raw image. In addition, the variation in alignment between the image sensor and fiber bundle with different pitches introduces a moiré pattern to the sensor response, independent of the captured scene. The moiré pattern can be partially compensated through flat-field calibration [8] but the lost resolution due to fiber-sensor gap and misalignment is not reversible with simple image calibration.

Various methods have been used to restore the image that was distorted by a stationary scattering medium. Turbid lens imaging for examples uses the transmission matrix of the scattering medium and wavefront shaping by exploiting spatial light modulators as well as angular spectrum decomposition to restore the image to the resolution limited by the numerical aperture (NA) of the imaging system [9]. This method and other similar methods [10-12] require a relatively complex characterization setup and the illuminating light source is primarily limited to a coherent one. Some methods require interferometric detection of the scattered image [9-11,13-15]. Incoherent light source and wavefront shaping [16] has also been used to restore the image off the scattering medium, but a spatial light modulator has to be used to reshape the scattering medium's wavefront.

The impulse response of a FC image sensor is strongly space variant due to irregularity and modal effect of individual fibers, and due to the irregular relative position between the individual fiber cores and the individual pixels of the image sensor. However, the impulse response should be constant. Therefore a sufficiently precise 2-D raster scan of the point spread function (PSF) with incoherent illumination

may provide the information needed to recover the lost resolution from the blurred lower resolution detected image. The advantages of this method are that it is not limited to monochromatic or coherent light, no wavefront shaping device is needed to characterize the imager or reconstruct the blurred image, and once the FC imager response is known it can be used to recover the lost information up to the fiber bundle pitch without adding complex elements to the system.

Because the system is not linear shift invariant (LSI), the use of shift-variant image restoration methods is essential. The signal to noise ratio (SNR) and the accuracy and repeatability of the PSF characterization are the limiting factors for faithful reconstruction of the image captured by a FC imager [17]. If the SNR of the imager is low, then both the input image and the characterized PSF are noisy, leading to inaccuracy in the image reconstructed by solving the inverse problem. If the PSF response changes, the characterization data is not accurate, further degrading the reconstructed image. In this paper, we characterize a fiber coupled image sensor, where light is transferred by a high spatial resolution (2.5 μm pitch) imaging fiber bundle to an attached (1.12 μm pitch) CMOS focal plane, and demonstrate reconstruction of the input image limited by the fiber bundle pitch.

The paper is organized as follows. Section 2 describes the characterization of the fiber-coupled image sensor, investigating SNR and repeatability of the highly shift-variant impulse response, and characterizing the response of a sub-pixel raster scan over a small region of interest of the sensor. We then consider the strongly shift-variant PSF data and show that LSI reconstruction methods such as deconvolution

cannot be applied for image restoration. In Section 3, we apply and compare several established linear and nonlinear shift-variant image reconstruction techniques on the sensed image data, showing that the processed image appears to reveal features of the fiber bundle not visible in the raw images. In Section 4, looking at images processed by the Iterative Expectation Maximization method, we confirm that the revealed fiber structure corresponds to the input fiber bundle itself, shown by microscopic inspection of the corresponding area at the input facet of FC sensor. Section 5 provides conclusions.

4-2 PSF Characterization of Highly Shift-Variant FC Imager

The resolution of imaging fiber bundles is limited by the refractive index contrast between the core and cladding of the fiber. As and example, refractive index of 1.81 and 1.48 is achieved for the core and cladding, respectively, with high performance (numerical aperture 1.0) 24AS fiber faceplate material provided by Schott Fiber Optics [18]. This limits the fiber bundle pitch to 2.5 μm for 70% fiber core fill factor (the ratio between the core area to the total area of the fiber bundle), where the cross-talk between fibers is still negligible. The fill factor can be further reduced to increase the fiber resolution while maintaining negligible cross-talk [5]. State of the art image sensors used in compact cameras have pixel pitches as low as

one micron. Figure 4-1(a) shows the OmniVision's 13351 monochrome image sensor, which has a 1.12 μm pixel. Attaching a 2.5 μm pitch fiber bundle to the 1.12 μm pitch image sensor [Figure 4-1(b)] limits the overall resolution of the imager to 2.5 μm. The schematic of the fiber bundle cross-section is shown in Figure 4-1(c) where the sensor grid (black rectangles) oversamples the straight fiber bundle (blue rectangles). The blue highlights represent fiber core area in the fiber bundle with 70% fill factor.

Figure 4-1(d) shows an example of the impulse response in a 12x12 pixel region of the bare monochrome image sensor in Figure 4-1(a), without fiber bundle or Bayer color filters. The impulse response was captured by placing a 25 μm pinhole in contact with the white LED light source at a long distance (2 meters) away from the image sensor. Absorptive color filters were used to narrow this light spectrum. A 50x microscope objective with NA of 0.55 was used to focus the light down to a pixel. While most of the energy is confined within one pixel of the image sensor, some background energy is detected in the adjacent pixels. This occurs due to the tail of energy in the Airy pattern of the optical probe that is created at the focus of the diffraction-limited microscope objective. The diameter of the diffraction limited spot size near the center of visible range at a wavelength of 550 nm is 1.22 μm, slightly larger than the sensor's 1.12 μm pitch.

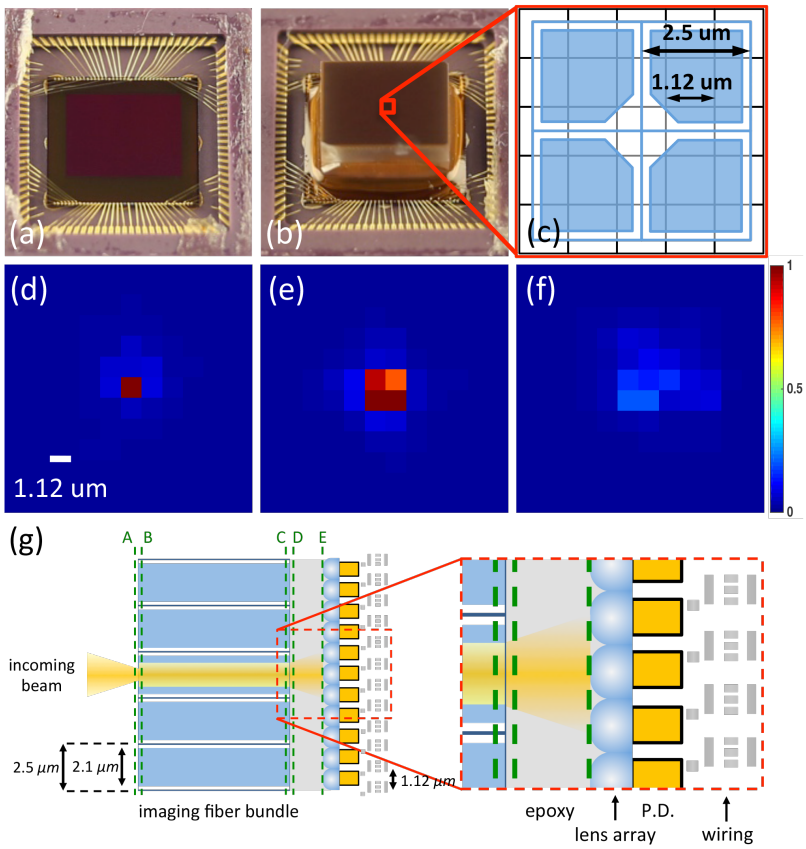

Figure 4-1 (a) OmniVision 13351 bare monochrome image sensor, (b) fiber coupled image sensor with 2.5 mm long fiber bundle attached, (c) schematic of the fiber bundle on top of the image sensor. A 12x12 pixels wide impulse response of (d) 1.12 µm pitch bare sensor, (e) FC image sensor with 2.5 µm pitch fiber attached to 1.12 µm pitch sensor with good fiber-sensor alignment and (f) same as (e) but with bad fiber-sensor alignment. (g) Schematics of the FC image sensor along the length of fiber bundle including the image sensor.

Figure 4-1(e) and Figure 4-1(f) show two representative samples of the PSF from the fiber-coupled image sensor [Figure 4-1(b)]. The best achievable PSF [Fig. 1(e)] is limited by the 2.5 µm fiber bundle and adhesive gap, which, as observed, yields a PSF restricted to an area of approximately 2x2 sensor pixels. When the illuminating point is positioned on the center of fiber, most of the energy is confined within the 2.1 µm width of the fiber core, which is close to twice the image sensor pitch (2.24 µm). Therefore, we expect the FC imager's PSF to be confined within a

2x2 pixels wide region at its best, consistent with observation. The PSF shape is highly shift-variant and nonuniform within this area due to the irregularity in fiber core shape, misalignment between fiber and the 2x2 pixels wide area and the modal effect of light transmission thought the fiber bundle. In the case where the input PSF lands on the fiber cladding or absorber material (used in the fiber bundle for elimination of background light), light is spread into more than one fiber and the detected PSF might spread wider than the 2x2 pixels limit [Figure 4-1(f)]. This strong variation of PSF along with the micron size gap between the backside of fiber bundle and the image sensor are the limiting factors of the resolution in FC imagers. In this case, shift-invariant image restoration methods such as deconvolution may not be applied to recover the lost data. However, if the shift-variant PSF map is known as a function of input location, then one can use shift-variant image restoration methods to recover the lost resolution.

The schematics of the FC image sensor cross section along the fiber bundle length is shown in Figure 4-1(g). The incident beam is focused on the surface of the fiber bundle on plane *A*. The resolution at this plane is limited by the performance of the system lens and it is considered to be linear shift-invariant, at least for a small field of view. The light is then coupled to the fiber bundle at plane *B*. The efficiency of coupling is determined by the location and angular spectrum of the incident beam, the surface roughness of the fiber bundle and the number of modes supported by each fiber. A multimode fiber with sufficiently large number of modes provides a more accurate sample of the incident beam. The coupled light then propagates to plane *C*. If

the cross-talk between fibers is low and the variation of fibers along the propagation direction is small, the propagation has little effect on the shape and intensity of the signal. The use of absorbing material in fiber bundle structure for cross-talk suppression usually leads to uniform attenuation of the signal [5]. The light emitted from the planar surface of the fiber bundle is transmitted into the epoxy layer at plane *D*. Note that while it is possible in principle to bond the fiber bundle directly to the surface of a CMOS sensor die, a few micron thick layer of UV-cured adhesive accommodates the differential thermal expansion of the glass and silicon. In cross-sections of such bonded fiber coupled sensors, we have achieved adhesive thicknesses ranging from 1.8 μm to 5 μm. The thicker the epoxy layer, the more blur in the image detected by the image sensor at plane *E*. The blur can be increased by misalignment between the center of the fiber core and the center of the pixel's active photodiode area. Therefore, the detected image at plane *E* is also not shift-invariant compared with the incident image at plane *A*.

The SNR of the overall imager and the repeatability of the PSF characterization determine the extent to which the lost data can be restored. Second order parameters such as sensor nonlinearity would also limit the accuracy of restoration process, but these effects are typically weaker and are not addressed here. An additional underlying assumption here is that PSF does not change over time either due to random mechanical stress or with environmental parameters such as temperature. For operation over a range of temperatures there will be thermal expansion, and the PSF will require characterization at several temperatures, to allow

generation of an interpolated PSF for the specific (measured) operating temperature, as was done for moiré compensation in [8].

The SNR of the imager can be estimated by selecting a flat region in the captured image and using the following estimation [19]:

$$SNR = 20\log_{10}\left(\frac{\mu_I}{\sqrt{\frac{1}{N}\sum_{i=1}^{N}(I_i-\mu_I)^2}}\right), \tag{8}$$

where I_i is the input image selected at a flat region, N is the number of samples (pixels), and μ_I is calculated from

$$\mu_I = \frac{1}{N}\sum_{i=1}^{N} I_i \,. \tag{9}$$

The SNR of the bare sensor, without fiber coupling, was estimated to be 35.3 dB at 10 ms integration time. The SNR of the FC imager would be much smaller if the RAW image is used directly without any calibration. Because the fiber bundle is strongly shift-variant, the standard deviation of the flat-field would be relatively large using Eq. (8). Instead, one can first calibrate the detected RAW image using the average of multiple flat-fields to compensate for the imperfect fill factor of the fiber bundle (70% core area in our case) and then apply the above equation to estimate the SNR of the FC imager. Using this calibration method, the SNR of the fiber-coupled imager was estimated to be 32.8 dB. The process of attaching the fiber bundle to the same image sensor thus reduces the SNR of the imager by 2.5 dB. A similar 2.4 dB

decline of SNR was observed using a 1 ms exposure time. This SNR estimate is used later for image reconstruction.

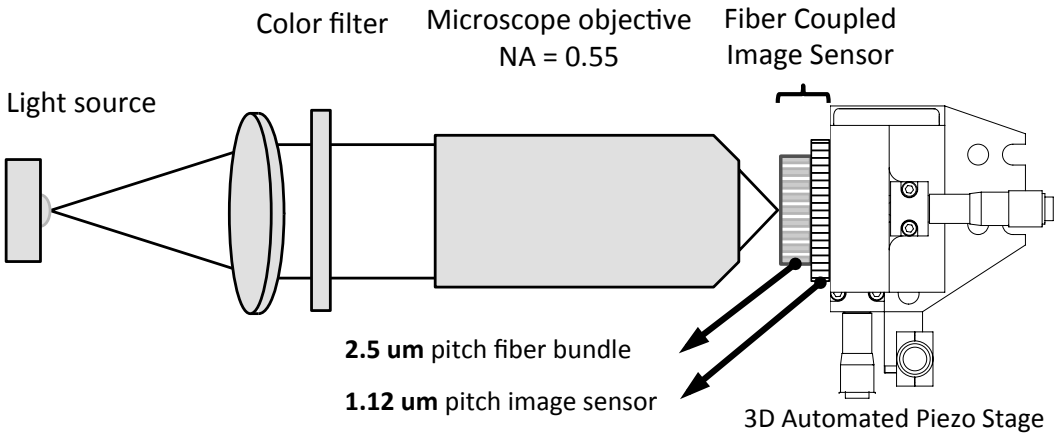

Figure 4-2 Schematic of the automated PSF characterization setup

Figure 4-2 shows the schematic of the PSF characterization setup. A 25 μm pinhole in contact with a white LED light source was used as the optical probe. An apochromatic microscope objective with NA of 0.55 was used to focus the optical impulse on the FC imager. Three broadband color filters were used to evaluate the effect of wavelength on the PSF and its repeatability. Hoya's 25A, X1 and 80A filters were used for red, green, and blue colors, respectively. It was also experimentally verified that PSFs captured by coherent (laser) light sources are highly variable and also limit the image reconstruction to a single wavelength. Incoherent light was used for the experimental results presented here. A 2.5 μm pitch and 2.5 mm long fiber bundle is attached to the bare monochrome image sensor without a color filter array. The FC image sensor is mounted on a computer-controlled Dali E-2100 piezo stage, which is used to capture the 2D PSF map on a limited area of the sensor. The position

can be varied with 20 nm steps, well below the 2.5 μm fiber or 1.12 μm image sensor pitches, or the 0.8 μm thickness of the low index cladding between fiber cores.

To verify the repeatability of the experiment the optical probe was scanned horizontally, and the resulting PSF was recorded as a function of the input location. The piezo stage was moved by 0.4 μm steps over a 10 μm range, and one PSF was captured at each step. An average of ten scans was taken to smooth out the random PSF variations (e.g. due to sensor noise). To avoid the piezo actuator hysteresis one can either reset the piezo's voltage to zero volts at the end of each X or Y scan, or use the position feedback to compensate for its inherent nonlinearity. Here we reset the voltage to zero volts and nonlinearly compensated the input voltage to linearize the position output. It is important to know the spacing between the sample points and convenient to have a constant spacing between them, otherwise the correlation between each captured PSF and the input probe location would be unknown.

Figure 4-3(a) and Figure 4-3(b) show the intensity value of two specific (grayed diagonal) pixels, along the scan line (color arrow) and off the scan line, respectively, for the light source with blue color filter. Here five 1D scans are compared, each being the average of ten horizontal scans. As one can see the measured average pixel values are fairly repeatable for various pixel locations. Similar trends were observed using the green color filter data in Figure 4-3(c) and Figure 4-3(d). Although the probe's 0.4 μm step size is lower than sensor's 1.12 μm pitch, the variation of pixel values is sensitive to submicron movements of the probe. This

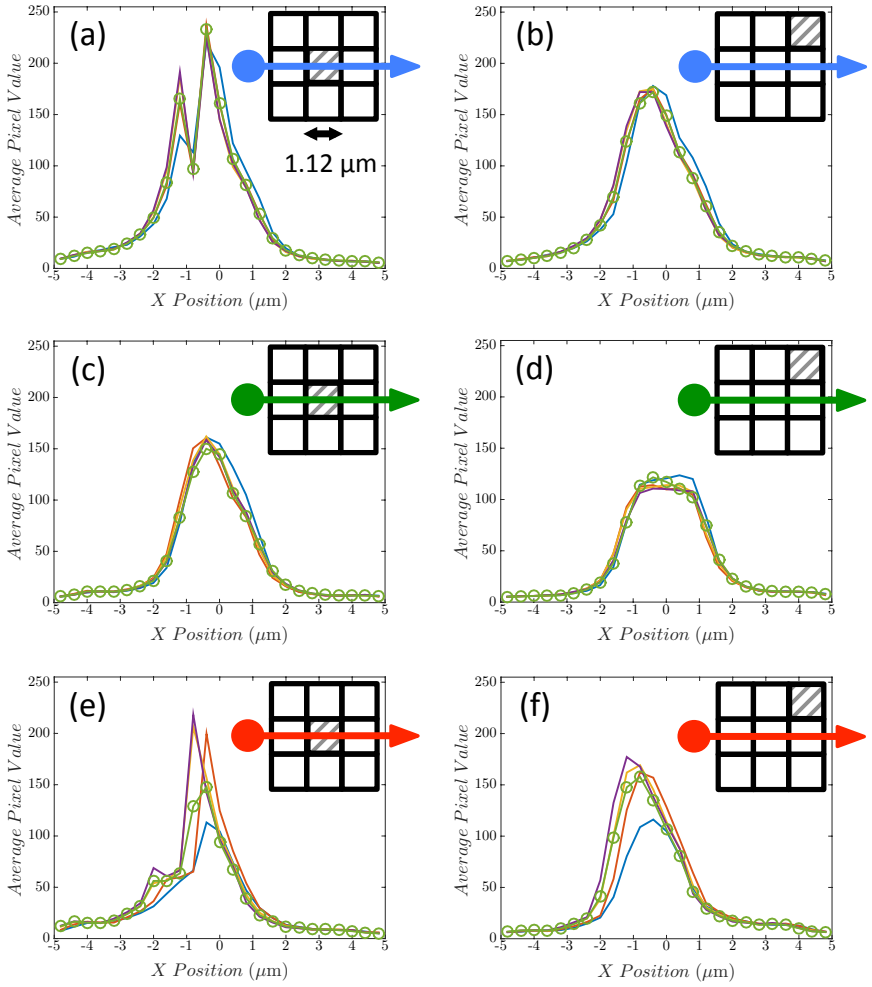

Figure 4-3 Repeatability of PSF measurements for average of ten 1D horizontal scans (color arrow) of the FC imager with blue color filter: (a) for a pixel located on the scan line (b) for a pixel located off the scan line. (c)-(f) same as in (a) and (b) repeated for green and red color filters, respectively.

strong shift-variance occurs because of light coupling to various modes of the fiber bundle, which carry different amounts of power as they propagate through the bundle.

A higher degree of repeatability is observed for blue and green color filters compared with the red color filter [Figure 4-3(e) and Figure 4-3(f)]. Stronger variations of the pixel values along the scan line result from longer transmitted wavelengths of the red color filter, larger diffraction-limited spot size, and further extension of guided modes

in the fiber bundle. The guided modes are more confined at shorter wavelengths and therefore less sensitive to the exact location of the input probe, which is approximately 1-1.3 μm wide in diameter. Likewise, the PSF repeatability of the white light is affected by the upper wavelength range of the LED source and therefore limits the accuracy of the measurements. The green color filter data is fairly repeatable and lies in the middle of visible range. From this point on we used this light source for both 2D PSF characterization of the imager, as well as capturing the resolution chart image for restoration. Similar results may be achieved with the blue color filter or any other light source that yields a repeatable PSF measurement. The repeatability curves in Figure 4-3(a-f) were measured by replacing the color filters and repeating the same line scan over the identical path. Therefore, the resulting curves may also be considered as the spectral response of the FC imager at a particular region of interest.

Having verified the repeatability of the measured data, the complete PSF data was captured as a function of input probe location. The shift-variant PSF map of the imager was captured as a function of input probe position by nonlinearly driving the piezo stage. Each line scan was followed by setting the Piezzo voltage to zero volts to avoid hysteresis. An area of 24x24 pixels wide (26.88 x 26.88 μm^2) was characterized using a step size of half the sensor pixel pitch (0.56 μm). The total number of PSFs is 47x47=2,209. The submicron step size is useful, as the fiber bundle cladding and absorber have comparable widths and the captured PSF is thus sensitive to these half-pixel-pitch displacements.

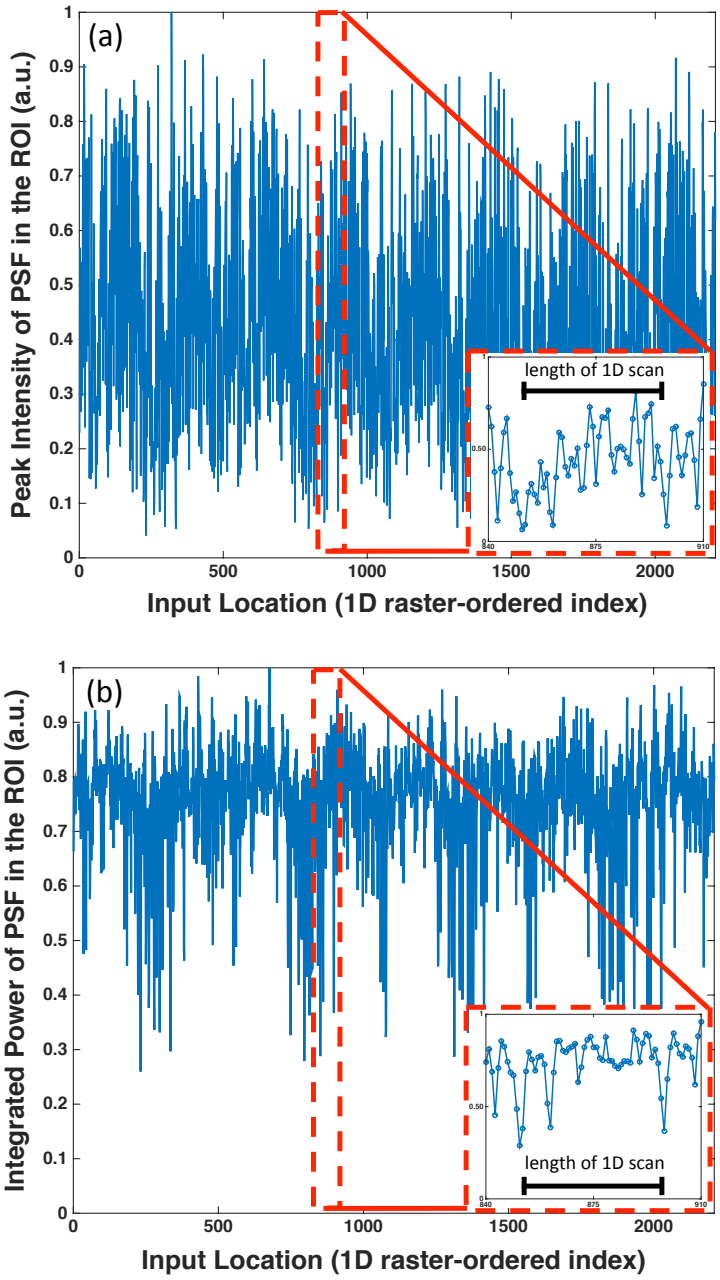

Figure 4-4 (a) Global peak intensity variation vs. input probe location (b) Total PSF power variation vs. input probe location.

Figure 4-4(a) and Figure 4-4(b) show the variation of the peak intensity (single pixel) and the integrated power of the entire 47x47 PSF region as a function of input probe location, respectively. Both peak intensity and integrated power vary strongly with

probe position. If the optical probe lands on the fiber core, the maximum intensity and power is transmitted. If the probe lands on the fiber cladding, light coupling is reduced and divided into multiple fiber cores. Finally landing the optical probe on the absorber material minimizes both transmitted intensity and detected power. The relative position of fiber cores and sensor pixels also contributes to stronger shift-variance of fiber coupled imagers.

In this case, linear shift-invariant assumption is not even remotely accurate, so shift-invariant restoration methods such as deconvolution cannot be applied for image reconstruction purposes. However, one can lexicographically order each of the captured PSFs into a column vector and form a PSF matrix H with each column representing one PSF and each row representing the position of input probe. The detected blurred image g can then be related to the original image f through the following equation:

$$g = Hf \ . \tag{10}$$

For simplicity, the detected 24x24 pixel image was bilinearly interpolated to match the input probe's 47x47 map. This way H becomes a 2209x2209 square matrix, and f and g are both 2209x1 column vectors. The characterized PSF matrix is shown in Figure 4-5. For a shift-invariant and sensor limited imager, H would become a diagonal matrix and Eq. (10) could be solved via deconvolution. However, in a fiber-coupled imager the individual fibers carry the input scene energy through multiple modes, which vary in shape and coupling coefficient. The modal effect of light transmission along with the imperfect fill factor of the fiber bundle (70%) results in

the shift-variant PSF matrix *H* that is not necessarily diagonal. In order to restore the lost resolution one has to use shift-variant image restoration methods. In the following section, we discuss several of these methods, and compare the image reconstructed using linear and nonlinear restoration methods.

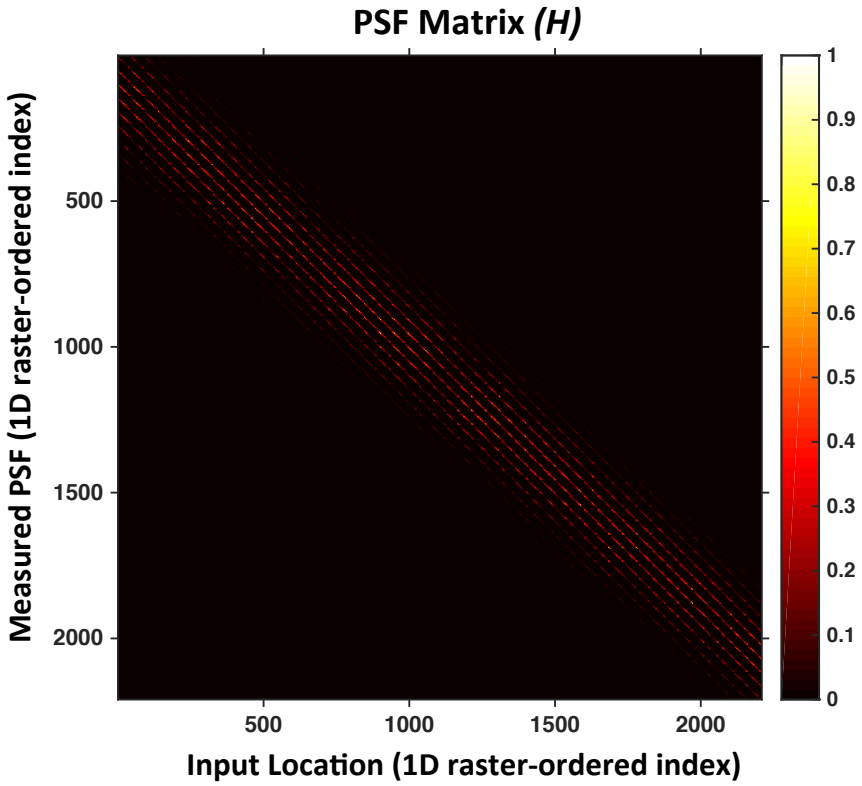

Figure 4-5 Experimentally characterized shift-variant PSF matrix (a.u.) for 2209 input probe locations.

4-3 Shift-Variant Image Restoration

The strong variation of the PSFs in fiber-coupled imagers suggests that conventional shift-invariant image restoration methods are not applicable. In this section, we examine a few of shift-variant image restoration methods. The

formulations are discussed in the first part and the reconstruction results are compared in the second part of this section.

4-3-1 Formulation

The PSF matrix H in Eq. (10) is ill-conditioned, and typically has zero determinant. Therefore, direct inversion of this matrix is not practical. However, one can use a generalized form of the inverse of H, or pseudo inverse of H to find the original image f. The Moore-Penrose pseudoinverse [20] is a well-known example:

$$f = H^{+} g \,, \tag{11}$$

where H^{+} is the pseudoinverse of H. Although the pseudoinverse matrix can exist and be unique, it usually yields a poor solution for f in Eq. (10). Instead one can solve the following non-negative least squares problem [21]:

$$\arg \min_{\hat{f}>0} \left\{ \| H\hat{f} - g \|_2^2 \right\}, \tag{12}$$

where $\hat{f}$ is the estimated restored image by solving Eq. (12) and $\|.\|_2$ signifies the L_2 or Euclidean norm. The least squares solution yields decent results for cases where the noise is insignificant. However, no prior information of the noise is used in the mathematical model given by Eq. (10), so in the presence of noise the result of reconstruction becomes less accurate. To improve the reconstruction result one may introduce the noise into the model:

$$g = Hf + n \,, \tag{13}$$

where n is the noise vector, and it is generally assumed to be additive Gaussian with zero mean. One way of solving Eq. (13) is to use Linear Minimum Mean Square Error (LMMSE) method to find the estimated solution by minimizing the error term $\epsilon = f - \hat{f}$. The LMMSE solution is then found by solving the following [22,23]:

$$\arg \min_{\hat{f}} E\left\{\varepsilon^T \varepsilon\right\} = E\left\{Tr\left(\varepsilon^T \varepsilon\right)\right\}, \tag{14}$$

where $E\{.\}$ and Tr denote the expected value operator and trace of a matrix, respectively. The solution requires knowledge of the autocorrelation matrix of the true image f, while in practice only the detected blurred image g is known. Another shortcoming of the linear restoration methods is the presence of negative pixel values in the reconstructed image. One way to overcome this limitation of the linear methods is to solve them iteratively. Tikhonov regularization [24,25] is widely used to solve Eq. (10) by introducing a regularization parameter and calculating the Euclidian norm of the solution or solving:

$$\arg \min_{\hat{f}} \left\{ \| H\hat{f} - g \|_2^2 + \lambda^2 \| C\hat{f} \|_2^2 \right\}. \tag{15}$$

Here C and λ are the regularization matrix and regularization parameter, respectively. Most common choices of C are the simple identity matrix, a diagonal weighting matrix or the first and second derivative operators [26]. Typical choices of the regularization parameter are the L-curve [27] and generalized cross validation [28] methods. The identity regularization matrix and L-curve method are used in this work. The solution to the above equation can be found in the following closed form:

$$\hat{f} = \left(H^T H + \lambda^2 C^T C\right)^{-1} H^T g \,. \tag{16}$$

To overcome the negative pixel values problem, one can nonlinearly solve the optimization problem given by Eq. (15) in an iterative fashion, by calculating the residual error at each iteration step. Non-negativity is achieved by imposing negative pixel values to be zero at each iteration step. This gives us the well-known Iterative Constrained Tikhonov-Miller (ICTM) restoration [25,29,30]. The minimum of the Tikhonov regularization functional in Eq. (15) is found by using the method of conjugate gradient [31]. The conjugate gradient direction d^k at k^{th} step is calculated from:

$$d^k = r^k + \alpha^k d^{k-1}, \tag{17}$$

where r^k is the steepest descent direction given by:

$$r^k = \left(H^T H + \lambda^2 C^T C\right)\hat{f} - H^T g\,, \tag{18}$$

and $\alpha^k = \left\|r^k\right\|_2^2 / \left\|r^{k-1}\right\|_2^2$. The subsequent iteration is obtained by calculating the following non-negative projection, where the negative image values are clipped to zero:

$$\hat{f}^{k+1} = \max(0, \hat{f}^k + \beta^k d^k)\,. \tag{19}$$

Without the non-negativity condition, f^{k+1} minimizes the Tikhonov functional in Eq. (15). Here the coefficient β^k is the optimal step size and its proper choice improves the convergence speed. Various methods can be used to find the optimal step

size. Some examples are the standard step size of the conjugate gradient method without the non-negative projection, the golden selection rule or first order Taylor expansion of Eq. (19) with respect to β^k [31,32]. Here we used the conjugate gradients method step size for constrained adaptive restoration. The explicit expression for optimal β^k is given by [30,33]:

$$\beta^k = \frac{\left(r^k\right)^T d^k}{\left\|Hd^k\right\|_2^2 + \lambda^2 \left\|Cd^k\right\|_2^2}. \tag{20}$$

The ICTM restoration yields converging non-negative result at the expense of more numerical complexity and lower computational efficiency. The iteration can stop when a threshold of relative error is reached. We used 1% relative error in this work, where it is defined as:

$$Err = \left\|f^{k+1} - f^k\right\|_2 / \left\|f^k\right\|_2. \tag{21}$$

Instead of using the L_2 norm regularization factor, one can introduce prior knowledge of the input scene sparsity by modifying the regularization term in Eq. (15) . Cao *et al.* [34] used the L_1 norm regularization to incorporate sparsity and solved the following optimization problem using Expectation Maximization (EM) [35]:

$$min\left\{\| H\hat{f} - g \|_2^2 + \gamma \| \hat{f} \|_1\right\}. \tag{22}$$

The non-negative projection is used at each iteration step to impose non-negativity. We will show that nonlinear restoration methods such as ICTM or non-negative expectation maximization are sufficient to restore the image to fiber-limited

resolution. In the following section we will compare the discussed methods for our image restoration application.

4-3-2 Experimental Restoration Results for Various Methods

The FC output image suffers from fiber artifacts as well as moiré pattern due to misalignment between the irregular fiber bundle and the image sensor with different pitches. Although flat-field calibration can partially compensate for fiber artifacts and the unavoidable moiré pattern, the lost resolution cannot be restored using this method. Figure 4-6(a) shows the detected RAW image by the FC imager in the 24x24 pixels region of characterization. The USAF resolution chart image was relayed through the microscope objective onto the FC sensor. As will be shown later, the fiber bundle is attached to the image sensor with a small tilt angle of ~5° between the pseudo-periodic fiber array and the image sensor array, resulting in the apparent sampling of the captured image to be tilted as well. The bilinearly interpolated RAW

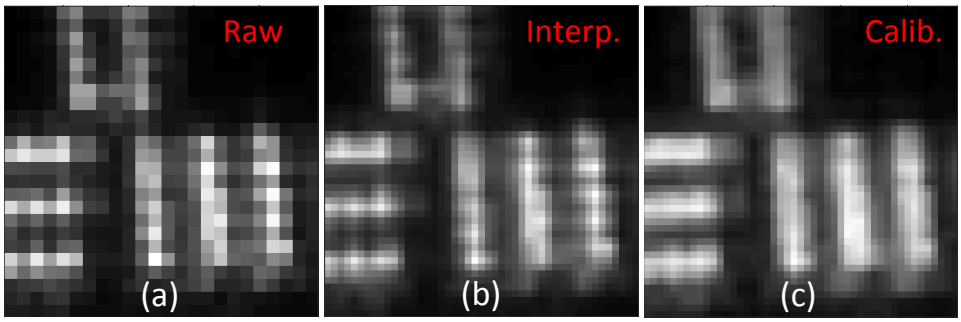

Figure 4-6 (a) Raw low-resolution image (b) High resolution image from bilinear interpolation of RAW image (c) Flat- field calibrated image.

image (47x47 pixels) and the result of flat-field calibration are displayed in Figure 4-6(b) and Figure 4-6(c), respectively. Although the flat-field calibrated image is visually smoother, the lost resolution in the blurred image is not recovered.

Once the FC imager is characterized in the region of interest, this information can be used along with the discussed image restoration methods to recover the lost resolution. Figure 4-7 compares various image restoration methods for Figure 4-6(a), starting from the worst. The trivial Pseudo-inverse restoration [Figure 4-7(a)] results in a completely distorted reconstructed image due to the large condition number ($\sim 10^{19}$) of the PSF matrix H. The least squares solution in Figure 4-7(b) poorly reveals the vertical bars of the resolution chart due to low SNR of the imager and excluding the noise from image restoration calculations. We introduced a Gaussian noise with zero mean into the restoration model and solved Eq. (14) to get the LMMSE estimate of the image [Figure 4-7(c)]. One problem with LMMSE is that prior knowledge of the true image's covariance matrix is needed. Here the detected image g was used instead. Another shortcoming with LMMSE and other linear restoration methods is the negative pixel values encountered after restoration.

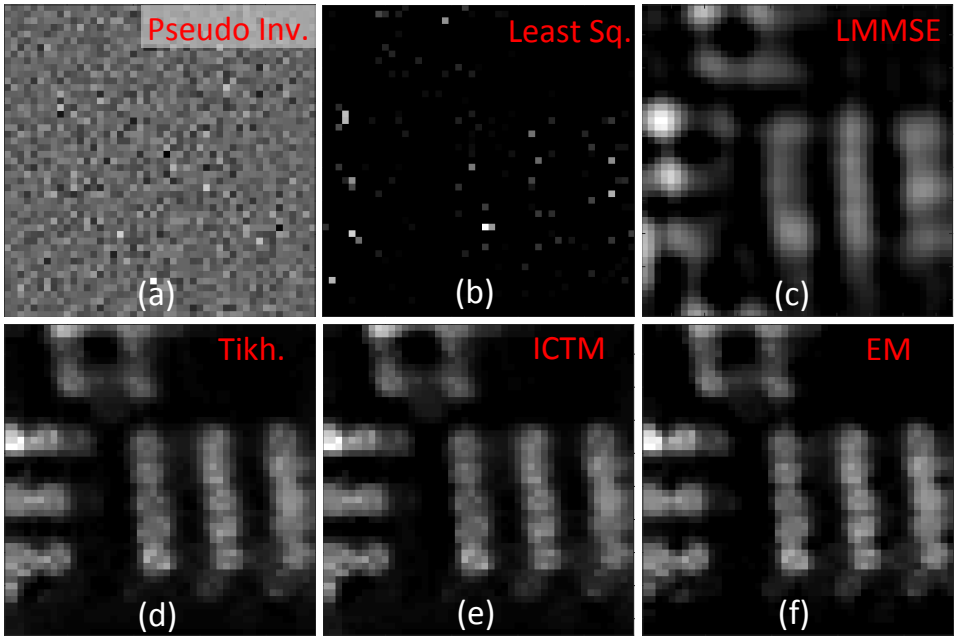

Figure 4-7 Results of image restoration using the experimentally characterized PSF matrix *H*: (a) Pseudo-inverse restoration, (b) non negative least squares restoration, (c) Linear Minimum Mean Square Error reconstruction with SNR 28 dB, (d) Tikhonov restoration and ignoring negative values, (e) Iterative Constrained Tikhonov-Miller restoration (<1% relative error), (f) Iterative EM restoration (<1% relative error).

To avoid the requirement for prior knowledge of the true image one can use the well-known Tikhonov restoration, in which a regularization parameter is used to enable image restoration from the ill-conditioned PSF matrix. The result of Tikhonov restoration is shown in Figure 4-7(d). The negative values were clipped to zero, however, further improvement may be achieved with ICTM method [Figure 4-7(e)] where the non-negative image is restored iteratively. Alternatively one can introduce sparsity as a prior knowledge and use expectation maximization to restore the blurred image iteratively as shown in Figure 4-7(f). Both ICTM and EM produce non-negative images that converge to 1% relative error defined by Eq. (21) within a few iterations. EM method is used for subsequent restoration of images.

4-4 Restoration to Fiber Resolution

A closer look at Figure 4-7(d-f) reveals what appears to be the fiber bundle structure, meaning that the image could be restored to that of fiber pitch resolution. Further improvement of the image resolution beyond the fiber pitch (close to the image sensor pitch) was not possible due to the low SNR of the imager and variations in the captured PSF.

In a similar experiment the USAF resolution chart was placed in contact with the FC image sensor. An index matching oil with refractive index of 1.6 was used in between to minimize scattering and image blur due to an unwanted gap. EM method was used to recover the lost resolution from the experimental PSF matrix *H*. Figure 4-8 shows the detected blurred RAW images on the top row and the result of iterative EM restoration on the bottom. Elements 5 and 6 of group 7 in the resolution chart were used to evaluate the performance of the FC imager and the experimental image reconstruction. Both input and restored images were gamma corrected with a coefficient of 1.4 for better visual appearance. A clear improvement in the resolution of the detected image is observed and the fiber bundle structure is once again observable in all of the restored images. The dark spots in the bottom right image reveal the cladding and absorber regions of the fiber bundle that are approximately of the size of less than a micron.

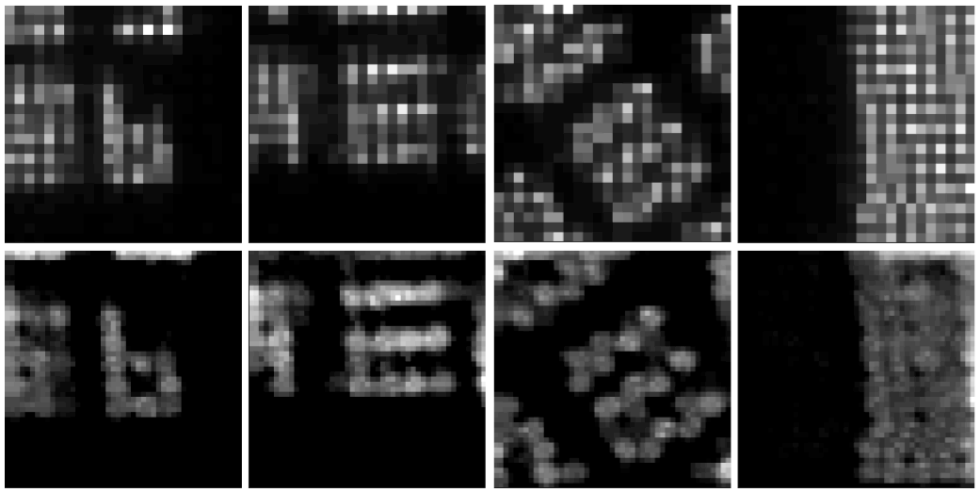

Figure 4-8 Reconstruction results for USAF res-chart in contact with FC imager. Top row: RAW detected images and bottom row: processed images using iterative EM method.

To verify that the observed fiber structures are not artifacts of the restoration process, a hexagonal aperture was imaged onto to the FC image sensor and a microscope image of the input facet of FC sensor was captured while it was closed down near the region of characterization [Figure 4-9(a)]. One can observe the irregular array of fibers with yellow cores and dark cladding and absorber regions. The fiber core boundaries in the region of interest (the red square in Figure 4-9(c)) were extracted from the microscope image by simple image processing. This process consists of converting the captured image to black and white, and registering the transition between black region and white regions as core boundaries. The same image was simultaneously captured by the FC image sensor [Figure 4-9(b)]. As one can see, individual fibers are not visible in the unprocessed RAW image; transmission through the adhesive gap between the output fiber bundle face and active sensing area has blurred the fiber structure. The captured image from the FC image sensor in the region

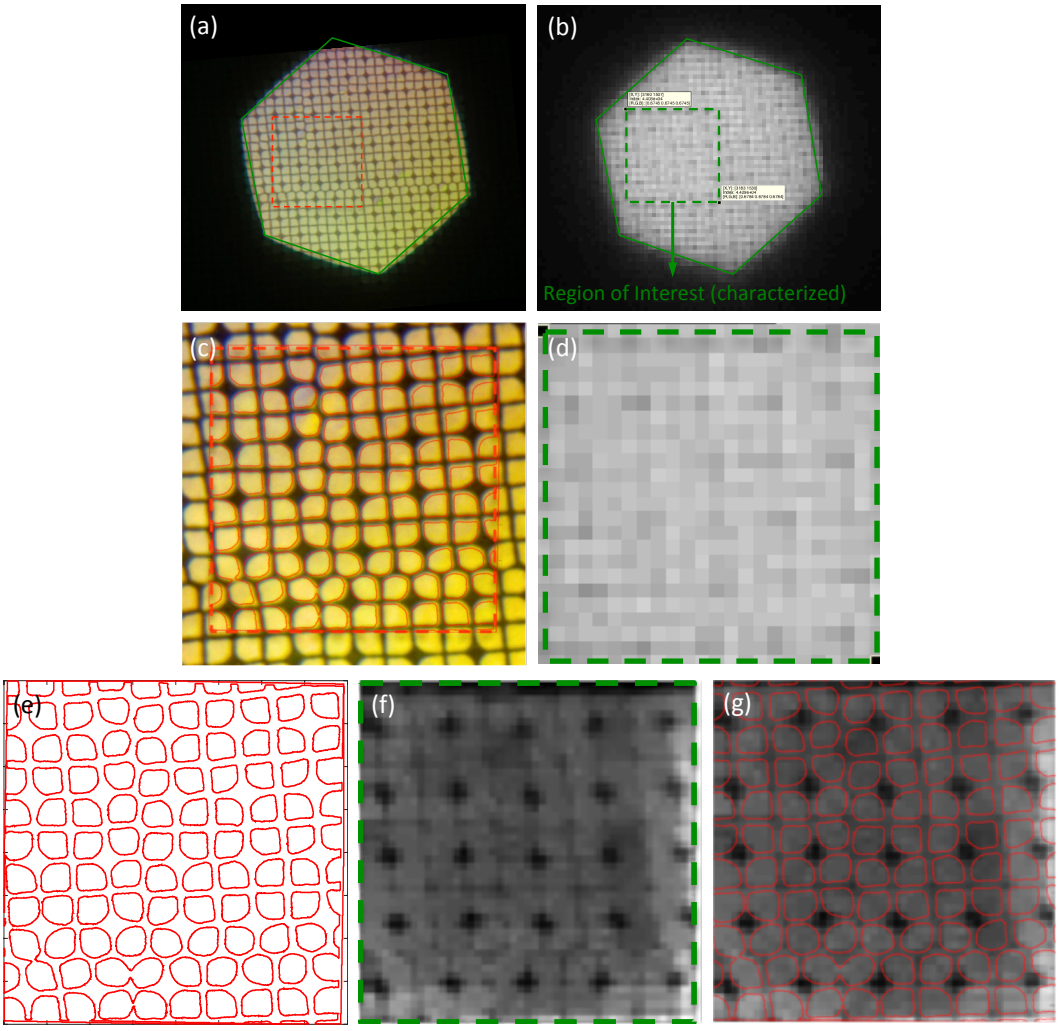

Figure 4-9 (a) Fiber bundle image captured by the microscope objective, (b) flat-field RAW image simultaneously captured by the FC image sensor, (c),(d) cropped region of interest from (a) and (b), respectively, (e) contour of core boundaries at the region of interest, (f) processed RAW image from FC image sensor at the same region, (g) contour of core boundaries superimposed on top of processed image of FC sensor.

of interest [Figure 4-9(d)] was processed using the EM restoration. The processed image [Figure 4-9(f)] clearly reveals details of the fiber bundle structure that is normally not detectable in the RAW image. Extracted core boundaries from the microscope image were then superimposed onto the processed image of FC sensor [Figure 4-9(g)]. The excellent match between the extracted core boundaries and the

fiber structure from the restored image confirms that with proper characterization and image processing, the blurred image in the FC imager can be restored up to the fiber pitch.

4-5 Conclusions

Fiber coupled imagers have strongly shift-variant impulse response due to the imperfect fill factor of the fiber bundle as well as the difference between the irregular fiber bundle pitch and the image sensor pitch. The misalignment between the fiber cores and individual pixels also contributes to the strong shift-variance. This strong shift-variance along with the inevitable spacing between the fiber bundle and the image sensor introduces image blur and loss of resolution. We experimentally characterized a region of interest in the FC image sensor to restore this loss of resolution. The measured PSF map was obtained by 2D scanning of the FC imager with a diffraction-limited microscope objective. Various shift-variant image restoration methods were compared to retrieve the lost resolution. Using iterative and nonlinear image restoration methods such as ICTM and EM, we were able to recover the lost resolution up to the fiber pitch. We also verified that the extracted fiber core boundaries from the microscope image match the fiber bundle structure that was obtained by proper image processing. Prior knowledge or control of environmental parameters may affect the quality of image restoration in these types of imagers. Further resolution improvement may be achieved, provided the PSF characterization is accurately repeatable and the FC imager has sufficiently high SNR.

Acknowledgments

Chapter 4, in part, has been submitted for publication of the material as it may appear in "Image restoration in fiber-coupled imagers using space-variant impulse response characterization", Motamedi, Nojan; Lomakin, Vitaliy; Ford , Joseph E. The dissertation author was the primary investigator and author of this paper.

This research was supported by the DARPA SCENICC program under contract W911NF-11-C-0210.We thank Dr. Mark A. Neifeld from University of Arizona and Dr. Ilya Agurok from Photonic Systems Integration lab at University of California San Diego for their invaluable discussions and suggestions. The bare monochrome Omnivision image sensors, and interface electronics, were provided by Google ATAP.

References

[1] T. S. Axelrod, N. J. Colella, and A. G. Ledebuhr, "The wide-field-of-view camera," Energy and Technology Review, 1-12 (1988).

[2] K. Itonaga, T. Arimura, K. Matsumoto, G. Kondo, K. Terahata, S. Makimoto, M. Baba, Y. Honda, S. Bori, and T. Kai, "A novel curved CMOS image sensor integrated with imaging system," in VLSI Technology (VLSI-Technology): Digest of Technical Papers, 2014 Symposium on, (IEEE, 2014), 1-2.

[3] T. Wu, S. S. Hamann, A. C. Ceballos, C.-E. Chang, O. Solgaard, and R. T. Howe, "Design and fabrication of silicon-tessellated structures for monocentric imagers," Microsystems & Nanoengineering **2**(2016).

[4] I. Stamenov, A. Arianpour, S. J. Olivas, I. P. Agurok, A. R. Johnson, R. A. Stack, R. L. Morrison, and J. E. Ford, "Panoramic monocentric imaging using fiber-coupled focal planes," Opt. Exp. **22**, 31708-31721 (2014).

[5] N. Motamedi, S. Karbasi, J. E. Ford, and V. Lomakin, "Analysis and characterization of high-resolution and high-aspect-ratio imaging fiber bundles," Appl. Opt. **54**, 9422-9431 (2015).

[6] N. Motamedi, A. Shlivinski, J. E. Ford, and V. Lomakin, "Efficient analysis of deep high-index-contrast gratings under arbitrary illumination," Opt. Exp. **23**, 33472-33483 (2015).

[7] S. Karbasi, I. Stamenov, N. Motamedi, A. Arianpour, A. R. Johnson, R. A. Stack, C. LaReau, R. Tenill, R. Morrison, I. P. Agurok, and J. E. Ford "Curved fiber bundles for monocentric lens imaging," in SPIE Optical Engineering+ Applications, (International Society for Optics and Photonics, 2015), 95790G-95790G-95797.

[8] S. Karbasi, N. Motamedi, A. Arianpour, W. M. Mellete, and J. E. Ford, "Analysis and compensation of moiré effects in fiber-coupled image sensors," in SPIE Optical Engineering+ Applications, (International Society for Optics and Photonics, 2015), 957910-957910-957918.

[9] Y. Choi, C. Yoon, M. Kim, W. Choi, and W. Choi, "Optical imaging with the use of a scattering lens," IEEE Journal of Selected Topics in Quantum Electronics **20**, 61-73 (2014).

[10] G. Oh, E. Chung, and S. H. Yun, "Optical fibers for high-resolution in vivo microendoscopic fluorescence imaging," Opt. Fiber Technol. **19**, 760-771 (2013).

[11] A. P. Mosk, A. Lagendijk, G. Lerosey, and M. Fink, "Controlling waves in space and time for imaging and focusing in complex media," Nature photonics **6**, 283-292 (2012).

[12] I. Vellekoop, A. Lagendijk, and A. Mosk, "Exploiting disorder for perfect focusing," Nature photonics **4**, 320-322 (2010).

[13] Y. Choi, T. D. Yang, C. Fang-Yen, P. Kang, K. J. Lee, R. R. Dasari, M. S. Feld, and W. Choi, "Overcoming the diffraction limit using multiple light scattering in a highly disordered medium," Physical review letters **107**, 023902 (2011).

[14] S. Popoff, G. Lerosey, R. Carminati, M. Fink, A. Boccara, and S. Gigan, "Measuring the transmission matrix in optics: an approach to the study and control of light propagation in disordered media," Physical review letters **104**, 100601 (2010).

[15] C.-L. Hsieh, Y. Pu, R. Grange, G. Laporte, and D. Psaltis, "Imaging through turbid layers by scanning the phase conjugated second harmonic radiation from a nanoparticle," Opt. Exp. **18**, 20723-20731 (2010).

[16] O. Katz, E. Small, and Y. Silberberg, "Looking around corners and through thin turbid layers in real time with scattered incoherent light," Nature photonics **6**, 549-553 (2012).

[17] W. H. Richardson, "Bayesian-based iterative method of image restoration," JOSA **62**, 55-59 (1972).

[18] "An Introduction to Fiber Optic Imaging," download available at http://www.us.schott.com/lightingimaging/english/download/fo.book.pdf.

[19] H. Liao, F. Li, and M. K. Ng, "Selection of regularization parameter in total variation image restoration," JOSA A **26**, 2311-2320 (2009).

[20] A. Albert, "Regression and the Moore-Penrose pseudoinverse," (1972).

[21] C. L. Lawson and R. J. Hanson, Solving least squares problems (SIAM, 1995), Vol. 15.

[22] A. C. Bovik, Handbook of image and video processing (Academic press, 2010).

[23] A. D. Hillery and R. T. Chin, "Iterative Wiener filters for image restoration," IEEE Transactions on Signal Processing **39**, 1892-1899 (1991).

[24] A. Tikhonov, "Solution of incorrectly formulated problems and the regularization method," in Soviet Math. Dokl., 1963), 1035/1038.

[25] A. N. Tikhonov and V. Y. Arsenin, "Solutions of ill-posed problems," (1977).

[26] P. C. Hansen, Rank-deficient and discrete ill-posed problems: numerical aspects of linear inversion (Siam, 1998), Vol. 4.

[27] P. C. Hansen, "Analysis of discrete ill-posed problems by means of the L-curve," SIAM review **34**, 561-580 (1992).

[28] G. H. Golub, M. Heath, and G. Wahba, "Generalized cross-validation as a method for choosing a good ridge parameter," Technometrics **21**, 215-223 (1979).

[29] K. Miller, "Least squares methods for ill-posed problems with a prescribed bound," SIAM Journal on Mathematical Analysis **1**, 52-74 (1970).

[30] R. L. Lagendijk and J. Biemond, Iterative identification and restoration of images (Springer Science & Business Media, 1990), Vol. 118.

[31] W. H. Press, S. A. Teukolsky, W. T. Vetterling, and B. P. Flannery, Numerical recipes in C (Cambridge university press Cambridge, 1996), Vol. 2.

[32] P. J. Verveer and T. M. Jovin, "Acceleration of the ICTM image restoration algorithm," Journal of Microscopy **188**, 191-195 (1997).

[33] R. Lagendijk, R. Mersereau, and J. Biemond, "On increasing the convergence rate of regularized iterative image restoration algorithms," in Acoustics, Speech, and Signal Processing, IEEE International Conference on ICASSP'87., (IEEE, 1987), 1183-1186.

[34] N. Cao, A. Nehorai, and M. Jacobs, "Image reconstruction for diffuse optical tomography using sparsity regularization and expectation-maximization algorithm," Opt. Exp. **15**, 13695-13708 (2007).

[35] T. K. Moon, "The expectation-maximization algorithm," IEEE Signal processing magazine **13**, 47-60 (1996).

Chapter 5 Conclusion and Discussion

Imaging fiber bundles and fiber-coupled image sensors were investigated in this thesis both numerically and experimentally. The main focus was on the specific application of fiber bundles for fiber-coupled imaging, in which, imaging fiber bundles are used to transform the curved image plane to the flat image sensor plane. The numerical modeling along with experimental characterizations helped us identify the factors affecting the cross-talk between fibers and enhance the resolution limit of the current imaging fiber bundles. A computational image processing approach was used at the end to further improve the resolution of the fiber-coupled imager with proper characterization of its space-variant impulse response.

The imaging fiber bundles were first treated as a 2D pseudo periodic grating and solved with RCWA. It was shown that an efficient numerical method can be used by modify the conventional RCWA solution in order to calculate the transmission of an electromagnetic beam through a deep dielectric grating. In this method the incident

beam was decomposed into its Fourier spectrum of plane waves and the propagating Bloch waves for the periodic grating region were calculated for each plane wave component using RCWA. The RCWA solution was simplified analytically by only considering the forward propagating Bloch waves and it was shown that there is an insignificant difference between the Global RCWA and Forward RCWA solutions for deep gratings. The variation of transmission coefficients with spatial frequency becomes faster as the grating depth increases, and therefore a larger number of samples is required for accuracy. Individual treatment of the propagating Bloch waves enabled us to calculate the inverse Fourier transform semi-analytically using both analytical integration of individual Bloch waves and FFT. The advantage was using the FFT to maintain the speed while accounting for the fast phase variations through analytical integration to maintain the accuracy of calculations with a smaller number of samples. It was shown that the presented formulations lead to accurate and efficient calculation of the output field.

Although efficient 2D modeling gives an insight into the performance of fiber bundles, it is not accurate enough to fully represent the 3D pseudo periodic imaging fiber bundles. Modal analysis was used for accurate 3D modeling of the extremely deep fiber bundles. The numerical investigation showed that a relatively small number of modes and guiding cores can be used for efficient modeling of the fiber bundles as a guide for fabrication of low cross-talk and high resolution imaging fiber bundles. As the fiber bundle's pitch scales down from 2.5 μm to 1.0 μm the performance of fiber bundles gets worse at the operating wavelength. This is explained by a lower

confinement and larger extension of guided modes into the cladding. This limits the resolution of the commercially available fiber bundle with numerical aperture of 1.0 to 2.5 μm. Using this numerical method, it was shown that reducing the fill fraction of the fiber cores increases the resolution of the fiber bundle. The numerical analysis also verified that introducing disorder or irregularity into the fiber bundle is crucial for improving the confinement and image resolution in fiber-coupled imagers. The accuracy of numerical modeling may be improved by using the actual fiber core boundaries in the model, which may be extracted by proper processing of the optical microscope or scanning electron microscope image of the fiber bundle cross-section.

The numerical modeling results were followed by experimental validation through characterization of fiber bundles. High resolutions fiber bundles were characterized using coherent and incoherent excitations. The measurements consisted of qualitative analysis of the image transported through different pitches of fiber bundles, impulse response characterization of a 2.5 μm pitch fiber bundle and finally quantitative analysis of the cross-talk with incoherent illumination. A good agreement was observed between the characterized impulse response of the fiber bundle and the numerical modeling results.

A methodology was proposed for improving the resolution of imaging fiber bundles, however, the fabrication difficulties associated with high index contrast multimode fibers limits the physical extent to which the performance may be enhanced. At this point, further improvement of the fiber bundle performance is only

feasible by computational processing of the image captured by the fiber coupled image sensor.

The impulse response of fiber coupled imagers is strongly shift-variant due to the imperfect fill factor of the fiber bundle as well as the difference between the irregular fiber bundle pitch and the image sensor pitch. The misalignment between the fiber cores and individual pixels also contributes to this strong shift-variance. This strong shift-variance along with the unavoidable spacing between the fiber bundle and the image sensor introduces image blur and loss of resolution. A region of interest in the fiber coupled image sensor was experimentally characterized to restore this loss of resolution. The PSF map was measured by 2D scanning of the fiber-coupled imager using a diffraction-limited microscope objective. Various shift-variant image restoration methods were then compared for retrieving the lost resolution. The resolution of the imager was recovered up to the fiber pitch using iterative and nonlinear image restoration methods such as ICTM and EM. It was also verified that the extracted fiber core boundaries from the microscope image match the fiber bundle structure that was obtained by proper image processing.

Coupled mode theory may be used for electromagnetic analysis of a larger array of fibers with less computational cost. However if the fibers are closely spaced, the modes of individual fibers vary in shape and the effective propagation indices vary in value, which may lead to inaccurate calculation of the coupled modes. Optimization of imaging fiber bundles using engineered and uncontrolled disorder is also a topic of further investigation. Further resolution improvement beyond the variation of physical

parameters may be achieved by computational image processing, provided the PSF characterization of the imager is accurately repeatable and the fiber-coupled imager has sufficiently high SNR.